DNA tensiometer reveals catch-bond detachment kinetics of kinesin-1, -2 and -3

Crystal R. Noell[1], Tzu-Chen Ma[1], Rui Jiang[1], Scott A. McKinley[2], William O. Hancock*[1,3]

[1] Department of Biomedical Engineering, Pennsylvania State University, University Park, Pennsylvania, USA
[2] Department of Mathematics, Tulane University, New Orleans, Louisiana, USA
[3] Department of Chemistry, Pennsylvania State University, University Park, Pennsylvania, USA

* Corresponding author
Email: woh1@psu.edu

Author Contributions: S.A.M. and W.O.H. conceived of original idea, C.R.N., R.J. and W.O.H. designed research; C.R.N., R.J. and T.M. performed research; C.R.N., T.M. and S.A.M. analyzed data; C.R.N., T.M., S.A.M., and W.O.H. wrote the paper.
Competing Interest Statement: The authors declare that they have no known competing financial interests or personal relationships that could have appeared to influence the work reported in this paper.

Abstract

Bidirectional cargo transport by kinesin and dynein is essential for cell viability and defects are linked to neurodegenerative diseases. The competition between motors is described as a tug-of-war, and computational modeling suggests that the load-dependent off-rate is the strongest determinant of which motor 'wins'. Optical tweezer experiments find that the load-dependent detachment sensitivity of transport kinesins is kinesin-3 > kinesin-2 > kinesin-1. However, when kinesin-dynein pairs were analyzed in vitro, all three kinesin families competed nearly equally well against dynein. One possible explanation is that vertical forces inherent to the large trapping beads enhance motor detachment. Because intracellular cargo range from ~30 nm to > 1000 nm, vertical forces in vivo are expected to range from near zero to larger than the horizontal forces of transport. To investigate detachment rates against loads oriented parallel to the microtubule, we created a DNA tensiometer comprising a DNA entropic spring that is attached to the microtubule on one end and a kinesin motor on the other. Surprisingly, kinesin dissociation rates at stall were slower than detachment rates during unloaded runs, a property termed a catch-bond. A plausible mechanism, supported by stochastic simulations, is that the strong-to-weak transition in the kinesin cycle is slowed with load. We also find evidence that the long run lengths of kinesin-3 (KIF1A) result from the concatenation of multiple short runs connected by diffusive episodes. The finding that kinesins form catch-bonds under horizontal loads necessitates a reevaluation of the role of cargo geometry in kinesin-dynein bidirectional transport.

Significance Statement

Kinesin and dynein motor proteins transport intracellular cargo bidirectionally along microtubule tracks, with the speed and directionality of transport involving a tug-of-war between the motor teams. We created a 'DNA tensiometer' that uses DNA as a spring to measure kinesin performance against loads oriented parallel to the microtubule. We find that dissociation rates paradoxically slow down with imposed loads. Dyneins are also thought to possess this 'catch-bond' behavior, meaning that both motors will hang on tightly during a tug-of-war. Previous work showed that combined vertical and horizontal loads cause faster detachment rates under load. Hence, we conclude that the effectiveness of kinesins during bidirectional transport depends strongly on the geometry of their cargo.

Introduction

Bidirectional cargo transport by kinesin and dynein is essential for cell viability, and disruptions in transport are linked to neurological diseases including hereditary spastic paraplegia, microencephaly and amyotrophic lateral sclerosis (Bilsland et al., 2010; Brenner et al., 2018; Caballero Oteyza et al., 2014; Makrythanasis et al., 2018; Millecamps & Julien, 2013; Moawia et al., 2017; Nicolas et al., 2018; Pant et al., 2022; Reid et al., 2002; Zhou et al., 2024). It has been established that kinesin and dynein, which move in opposite directions along microtubules, are often bound simultaneously to the same cargo (Encalada et al., 2011; Hendricks et al., 2010; Soppina et al., 2009; Welte, 2004). However, the mechanisms by which the motors compete and coordinate their activities to achieve proper directional transport are still poorly understood.

The prevailing model for bidirectional transport along microtubules is the 'tug-of-war' model, which posits that when kinesins and dyneins are both bound to the same cargo, the cargo will be transported in the direction of the strongest motor team (Belyy et al., 2016; Gross, 2004; Hancock, 2014; Hendricks et al., 2010; Muller et al., 2008). Evidence supporting this model includes the elongation of intracellular cargoes just before directional switching (Soppina et al., 2009), and computational modeling that predicts back-and-forth cargo movement similar to the vesicle dynamics observed in cells (Hendricks et al., 2010; Muller et al., 2008). Paradoxically, other studies have shown that knockdown of one motor results in a reduction of transport in both directions, a result not explained by the tug-of-war model (Gross et al., 2002; Hancock, 2014; Kunwar et al., 2011; Martin et al., 1999), and indicating there may be additional regulatory proteins or coordination between the motors either directly or via adaptor proteins.

Intuitively, a motor's effectiveness in a tug-of-war rests on its ability to remain bound to its microtubule track. Consistent with this, computational simulations have found that the load-dependent off-rate of a motor is the most important determinant of whether it wins or loses in a tug-of-war (Ma et al., 2023; Ohashi et al., 2019). Simply put, motors that remain attached under load beat motors that readily detach under load. Single-bead optical tweezers have found that the transport motors kinesin-1, -2, and -3 all act as slip bonds, defined as load accelerating their detachment rate. Their propensity to detach under load was determined to be: kinesin-3 > kinesin-2 > kinesin-1 (Andreasson, Milic, et al., 2015; Andreasson, Shastry, et al., 2015; Budaitis et al., 2021; Pyrpassopoulos et al., 2023; Tomishige et al., 2002). Based on this slip-bond behavior, it was surprising that when kinesin-1 was linked to dynein, the complex moved at near-zero speeds for up to tens of seconds, much longer than predicted based on previously measured kinesin-1 off-rates (Andreasson, Milic, et al., 2015; Feng et al., 2020; Yildiz et al., 2008). Moreover, a subsequent study found that kinesin-1, -2, and -3 all fared equally well against dynein, contrary to predictions from single-bead optical tweezer measurements that found differing load-dependent detachment rates (Gicking et al., 2022).

A pair of recent theoretical and experimental studies suggested a potential solution to this paradox, namely that the ~micron scale beads used for optical trapping result in significant forces oriented perpendicular to the microtubule as the motor pulls against the force of the trap (Howard & Hancock, 2020; Pyrpassopoulos et al., 2023; Pyrpassopoulos et al., 2020). In support of this, when a three-bead geometry was used

(in which the motor is raised up on a pedestal bead and the microtubule was held by beads attached to either end of the microtubule) motors remained bound longer than in the single-bead geometry (Pyrpassopoulos et al., 2023; Pyrpassopoulos et al., 2020). In cells, kinesin and dynein transport cargo that range from tens of nm in diameter (like vesicles), where motor forces are expected to be aligned parallel to the microtubule, up to several microns (like mitochondria and nuclei), where vertical forces are expected to be much larger. Thus, understanding the influence of vertical and horizontal forces on transport motors is important for understanding the mechanics underlying bidirectional transport in cells.

The goal of the present study was to characterize the load-dependent detachment kinetics of kinesin-1, -2 and -3 motors in a geometry that eliminates vertical forces inherent in traditional optical trapping studies. We achieved this by using double stranded DNA (dsDNA), which acts as an entropic spring to resist the pN-level forces generated by the motors (Iwaki et al., 2016; Marko & Siggia, 1995). In this DNA tensiometer, one end of a micron-long (3 kb) strand of dsDNA is bound to the microtubule and the other end to a quantum dot (Qdot)-labeled motor. Motors stretch the DNA spring until reaching stall and remain there until slipping back or detaching from the microtubule. We found that kinesin-1, -2, and -3 all remained at stall for multiple seconds before releasing, which is substantially longer than the unloaded run times for kinesin-1 and -2. This behavior of slower off-rates under load is defined as a 'catch bond' and contrasts with the normal 'slip bond' behavior load-accelerated off-rates seen previously for kinesin (Thomas et al., 2008).

Results

Constructing a motor-bound DNA tensiometer

To study motor performance against a resistive load oriented parallel to the microtubule, we constructed a DNA tensiometer consisting of a ~ 1 μm strand of dsDNA attached to the microtubule on one end and a motor on the other (Figure 1A). We used TIRF microscopy to visualize the motor moving against the entropic elasticity of the DNA spring. Due to the nonlinear elasticity of the DNA (Figure 1B) (Iwaki et al., 2016; Marko & Siggia, 1995), the motor moves under minimal load until it stretches the DNA to near its contour length, at which point it stalls (Figure 1C-E).

Our DNA-motor tensiometer consists of a 3,009 bp (999 nm contour length) dsDNA 'spring' that was synthesized by PCR using a biotinylated forward primer for attachment to the microtubule and a reverse primer containing a 3' overhang for motor attachment (details in Methods). We investigated members of the three dominant families of kinesin transport motors, kinesin-1 (*Drosophila melanogaster* KHC), kinesin-2 (*Mus musculus* Kif3A), and kinesin-3 (*Rattus norvegicus* Kif1A) used in our previous kinesin-dynein study (Gicking et al., 2022). In each case, the motor and neck linker domains were fused to the stable neck-coil domain (residues 345-406) of kinesin-1, followed by EGFP, a SNAP tag, and His_6 tag, as described previously (Gicking et al., 2022). Motors were conjugated to an oligonucleotide complimentary to the 3' overhang of the dsDNA spring via their C-terminal SNAP tag. The DNA tensiometer complex (Figure 1A) was created in a flow cell by sequentially flowing in biotinylated

microtubules, neutravidin, biotinylated dsDNA, and Qdot-functionalized motors containing the complimentary oligo (described fully in Methods).

The resulting dsDNA tensiometer kymographs (Figure 1C) show a reproducible behavior of moving, stalling, and returning to origin multiple times, which contrasts with the singular attachment, unidirectional movement and detachment of motors not bound by DNA (Figure S1). Because motors are tethered to the microtubule by the flexible DNA, large fluctuations around the origin are observed when the motor is detached (Figure 1C-H). Consistent with these fluctuations, initial attachment points were variable and roughly normally distributed with a standard deviation of 145 nm (Figure S2). Upon attachment to the microtubule, the motor walks at a steady velocity, consistent with the expected nonlinear stiffness of the dsDNA tether (Figure 1B), until it either detaches and returns to origin or reaches a stall state. Stalls end in three possible ways: 1) the motor slips a short distance (defined as a minimum distance of 60 nm from the stall point to greater than 400 nm from the origin) and immediately begins moving again; 2) the motor returns to the baseline and rapidly (within 100 ms) begins a new ramp; or 3) the motor returns to the baseline and fluctuates around the origin (generally for a few seconds), before binding and initiating a new ramp (Figure 1E). These three classes of features were seen in all three motors (Figure 1F-H and Figure S3).

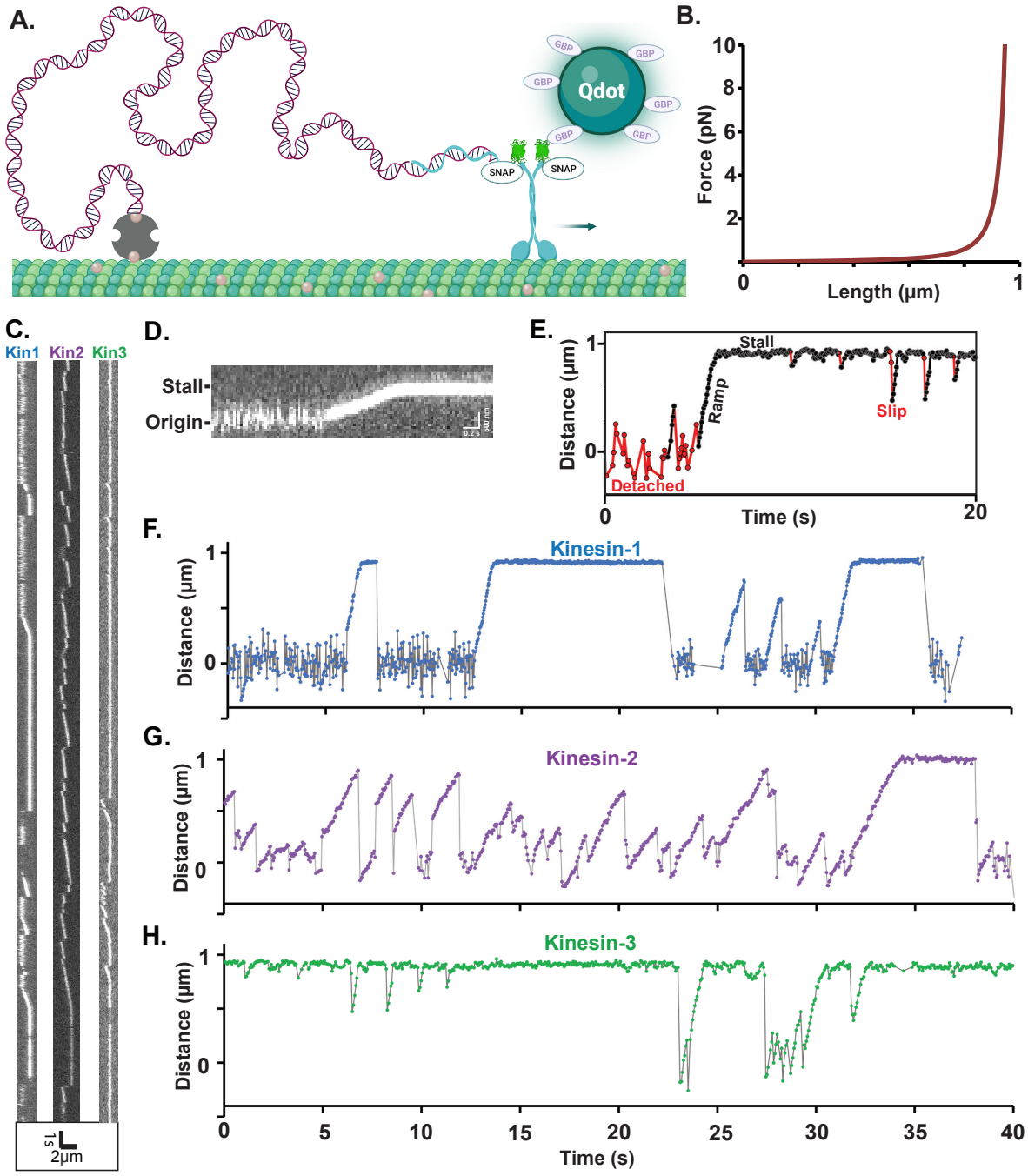

Figure 1. Experimental Design and Raw Data from Motor-DNA Tensiometers. (A) Schematic of a motor-DNA tensiometer, consisting of a dsDNA (burgundy) connected on one end to a kinesin motor through a complimentary oligo (blue), and on the other end to the MT using biotin-avidin (tan and gray, respectively). A Qdot functionalized with GFP binding protein nanobodies is attached to the motor's GFP tag and used to track motor position. (Not to scale; motor and Qdot are both ~20 nm and DNA is ~1 micron) (B) Predicted force extension curve for a worm-like chain 3009 bp dsDNA based on a 50 nm persistence length. (C) Representative kymographs of motor-DNA tensiometers for kinesins-1, -2 and -3. (D) Enlarged kymograph showing diffusion around the origin, ramp, and stall. (E) Example distance vs. time trace (kinesin-3), highlighting detached durations (red), ramps and stalls (black) where the motor has

pulled the DNA taut, and transient slips during stall (red). (F-H) Representative distance vs. time plots for kinesin-1 (F), kinesin-2 (G) and kinesin-3 (H), corresponding to the kymographs in (C). Further examples are shown in Figure S3.

Kinesin-1 and -2 act as catch-bonds at stall

The first question we addressed was: what are the detachment rates of kinesin-1, -2 and -3 motors at stall? During a tug-of-war with dynein, kinesins are expected to be at or near their stall force, and the ability of the motor to resist detachment is the major determinant of whether kinesin or dynein prevails in the tug-of-war (Ma et al., 2023; Ohashi et al., 2019). The load-dependence of protein-protein interactions can be described by one of the following mechanisms: a slip-bond (Bell, 1978), defined as a faster off-rate under load; an ideal bond, defined as an off-rate that is independent of load; or a catch-bond, in which the off-rate is slower under load (Thomas et al., 2008). Single-bead optical trapping studies consistently find slip-bond characteristics for kinesin-1, 2 and 3 (Andreasson, Milic, et al., 2015; Andreasson, Shastry, et al., 2015; Budaitis et al., 2021; Rao & Gennerich, 2022), whereas dynein off-rates have been described as a slip-bond or catch-bond (Ezber et al., 2020; Kunwar et al., 2011; Rai et al., 2013; Sanghavi et al., 2021; Soppina et al., 2009).

We define stall duration as the time that a motor stalls against the hindering load of fully extended DNA, without further detectable stepping, before detaching (Figure 1E). We don't directly measure the stall force, however, based on the predicted force-extension curve of the dsDNA (Figure 1B), the displacements are consistent with the 4-6 pN stall forces for kinesin-1, -2 and -3 measured using optical traps (Blehm et al., 2013; Budaitis et al., 2021; Kojima et al., 1997; Schroeder et al., 2012; Svoboda & Block, 1994; Visscher et al., 1999). Stall durations were compared to the unloaded single-motor run durations determined from TIRF kymograph analysis (Figure S1).

To compare unloaded to stall off-rates, cumulative distributions of the run and stall durations were plotted for each motor and fit with a single exponential function (Figure 2). The kinesin-1 tensiometer stall duration time constant was 3.01 s, with 95% confidence intervals (CI) of 2.30 to 3.79 s determined via bootstrapping in MEMLET with 1000 iterations) (Woody et al., 2016) (N= 78 stalls). In contrast, the kinesin-1 unloaded run duration time constant, measured by a traditional TIRF assay, was 1.04 s, (95% CI of 0.79 to 1.30 s; N= 59) (Figure 2A). Stall durations longer than unloaded run durations indicate that load slows the off-rate, the definition of a catch-bond (Thomas et al., 2008). Similarly, the kinesin-2 tensiometer stall duration time constant of 2.83 s (95% CI of 2.03 to 3.79 s; N= 50) was longer than its unloaded run duration of 1.07 s (95% CI of 0.85 to 1.35 s; N= 87) also indicating a catch-bond. Conversely, the kinesin-3 tensiometer stall duration time constant of 1.89 s (95% CI of 1.53 to 2.31 s; N= 140) was shorter than its unloaded run duration of 2.74 s (95% CI of 2.33 to 3.17 s; N= 106), indicating a slip-bond characteristic by this definition.

In this analysis, we defined transient slips as short as 60 nm as terminations of stall plateaus (Figure 1E). This is a stringent limit because motors rapidly reestablished stall after these slips, and in the context of a tug-of-war, these motors functionally remain attached to the microtubule. Thus, we reanalyzed the stall durations where slips are not defined as terminations of stall plateaus and found that all three motors had substantially longer stall durations (Figure S4). In particular, the kinesin-3 stall duration in this analysis was longer than its unloaded run duration, defining it as a catch-bond by

this measure. Finally, to rule out the possibility that the long stall durations were caused by more than one motor binding to the Qdot (despite the 1:10 motor: Qdot mixing ratio), we removed Qdots from the assay entirely and instead incorporated Cy5-dCTP into the dsDNA to visualize tensiometer extensions. This assay produced similarly long stall durations (Figure S5), confirming that the long stalls were caused by single motors.

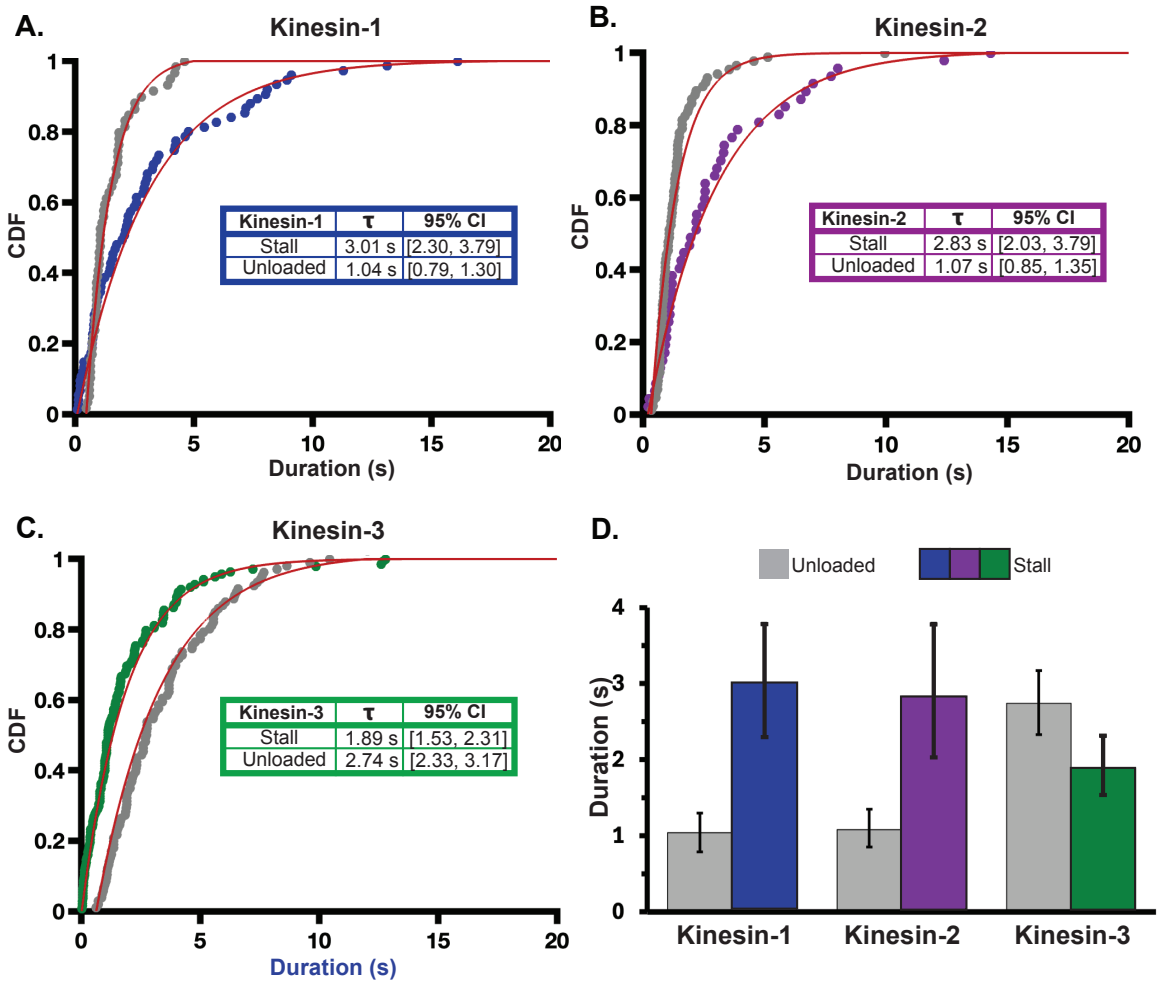

Figure 2. Tensiometer Stall Durations Indicate Catch-bond Behavior for Kinesin-1 and -2. Tensiometer stall durations are plotted for A) kinesin-1 (blue), (B) kinesin-2 (purple), and (C) kinesin-3 (green). Unloaded run durations for each motor are plotted in gray. Distributions were fit with a single exponential function using MEMLET to generate time constants, representing the mean durations, and 95% confidence intervals (CI), given in inset tables. (D) Bar plot indicating the difference between unloaded and stall times for the three motors with error bars indicating 95% CI. Stall durations >20s were excluded from the fit (there were three >20 s stalls for kinesin-1 and two >20 s stalls for kinesin-2). A bi-exponential fit of all data is shown in Figure S6.

Kinesin-3 detaches readily under low load

To determine whether sub-stall hindering loads affect motor detachment rates, we compared tensiometer ramp durations to the tensiometer stall and unloaded run durations (Figure 3). Although the dsDNA force extension curve (Figure 1B) predicts

negligible loads until the DNA is close to fully extended, there are still non-zero loads imposed during the ramp phase that may affect motor detachment. We defined ramp durations as the time the motor spends walking against the DNA spring, where 'failed' ramps are terminated by detachment and 'successful' ramps are terminated by reaching stall. To estimate the true detachment rate during the ramp phase in a way that takes into account both the successful and failed ramps, we used a Markov process model, coupled with Bayesian inference methods (detailed in Supplementary Material). In this model, each increment of time is considered to be an independent opportunity to detach while assuming a constant detachment rate. Using the notation τ for the duration parameter, the probability of staying attached to the microtubule through a segment of duration Δ is $e^{-\Delta/\tau}$. Using this method, ramp duration parameters, τ, were calculated for each motor, along with 95% credible regions. Finally, to allow for proper comparison, we performed a similar analysis to obtain the stall and unloaded duration parameters along with their 95% credible regions (Figure 3). The stall and unloaded durations were similar to estimates from curve fitting in Figure 2 (Table S1).

The simplest prediction is that against the low loads experienced during ramps, the detachment rate should match the unloaded detachment rate. However, each of the three motors had a unique relationship between their unloaded and ramp durations (Figure 3, Tables S3 and S4). The simplest case was kinesin-2, where the ramp duration of 0.97 s was within 95% CI of the unloaded run duration of 1.08 s (Figure 3B). In contrast, the kinesin-1 ramp duration of 2.49 s was much closer to the stall duration (3.05 s) than the unloaded run duration (1.05 s) (Figure 3A). The simplest interpretation is that the catch-bond character of kinesin-1 engages at low loads rather than rising proportionally to load or engaging only near stall (see Discussion).

The most notable ramp behavior was seen in kinesin-3, where the ramp duration of 0.75 s was nearly four-fold shorter than the unloaded run duration (2.76 s) and was more than two-fold shorter than the stall duration (1.90 s) (Figure 3C). As expanded on in the Discussion, the positively charged 'K-loop' in the kinesin-3 motor KIF1A is known to interact electrostatically with the negatively charged C-terminal tail of tubulin (Soppina et al., 2022; Zaniewski et al., 2020; Zaniewski & Hancock, 2023); thus, it is reasonable that even the low loads imposed during ramps are sufficient to overcome these weak electrostatic interactions. Notably, by defining the ramp duration as its behavior under low load, kinesin-3 can be classified as a catch bond because high load (stall) durations are longer than low load (ramp) durations.

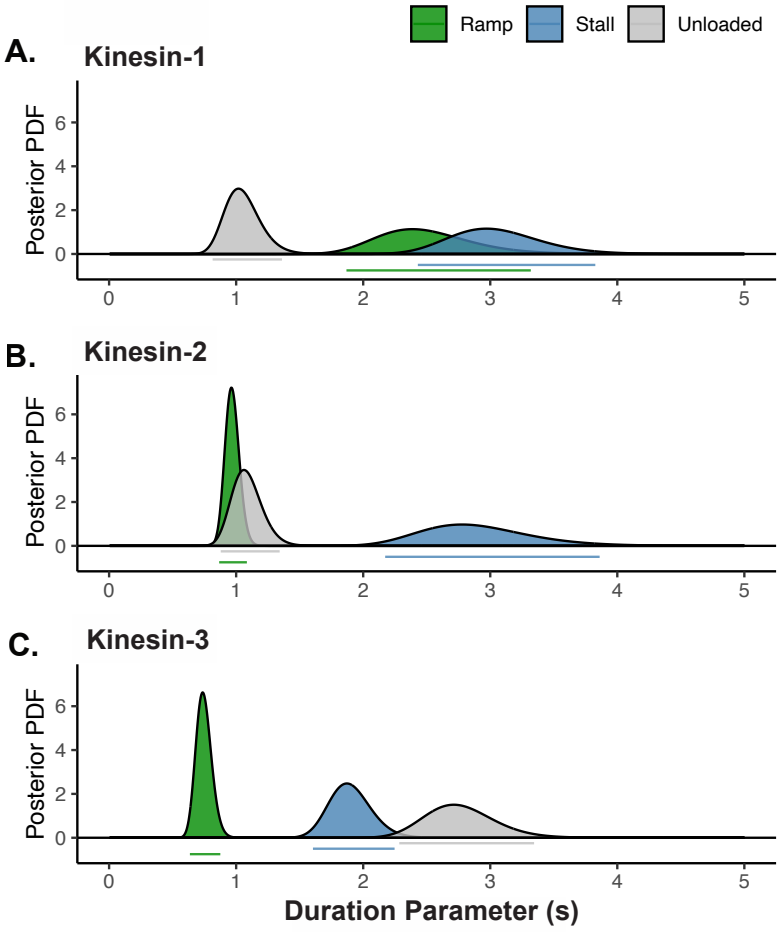

Figure 3. During Ramps, Kinesin-3 Detaches More Readily Than Under Zero Load. Unloaded, ramp, and stall duration parameters were estimated using a Markov process model, coupled with Bayesian inference methods. Curves show the posterior probability distributions of the duration parameters for (A) kinesin-1, (B) kinesin-2 and (C) kinesin-3. Bars below each peak indicate the 95% credible regions for the ramp (green), unloaded (gray) and stall (blue) duration parameters. Notably, the estimated ramp durations are larger, the same, and smaller than the unloaded run durations for kinesin-1, -2, and -3, respectively. For the unloaded and stall durations, this estimation method produces almost identical values as the maximum likelihood estimates in Figure 2 (values provided in Table S1).

Kinesin-3 reattaches more rapidly than Kinesin-1 and Kinesin-2

In the cell, motor-microtubule binding events include both the initial attachment of a freely diffusing motor-cargo binding to the microtubule, or it can involve a cargo-bound motor undergoing a constrained diffusion near the microtubule before rebinding to the filament. Our tensiometer geometry roughly encompasses both of these extremes; unbound motors diffusing on a ~1 um long DNA tether mimics free diffusion, whereas transient slips are so short that the motor likely remains weakly associated with the microtubule before reengaging (Figure 1C-H). To compare the behaviors of the three motors, we distinguished three types of reattachment events: 1) slow reattachments in which the motor returns to the baseline and fluctuates diffusively before rebinding to the

microtubule; 2) rapid reattachments in which the motor detaches from a ramp or stall, returns to the origin, and immediately (within ~0.1 s) begins walking again from origin; and 3) slips, in which a motor at stall detaches and before it can make it back to origin (>60 nm from the stall plateau and >400 nm from origin), it quickly reattaches within a single frame (~0.04 s) and begins walking again.

We first plotted all reattachment times as cumulative distributions and fit the data with a bi-exponential to separate out fast from slow events (Figure 4A). All three motors were fit by a fast time constant and a slow time constant with roughly similar amplitudes. One notable feature was that the three motors had different slow durations, with kinesin-1 > kinesin-2 > kinesin-3. This sequence qualitatively matches the relative bimolecular on-rates measured previously by stopped-flow but the quantitative differences here are much more subtle than the >10-fold range measured in solution (Chen et al., 2015; Feng et al., 2018; Zaniewski et al., 2020). Next, we compared the relative fractions of slips and fast and slow reattachments for each motor (Figure 4B with example kymographs of each type of event). The most notable feature is that kinesin-3 had the highest proportion of slip events. This result matches what was seen previously in a three-bead optical trapping assay that had higher time resolution and found that the majority of slip events recovered within 2 ms (Pyrpassopoulos et al., 2023).

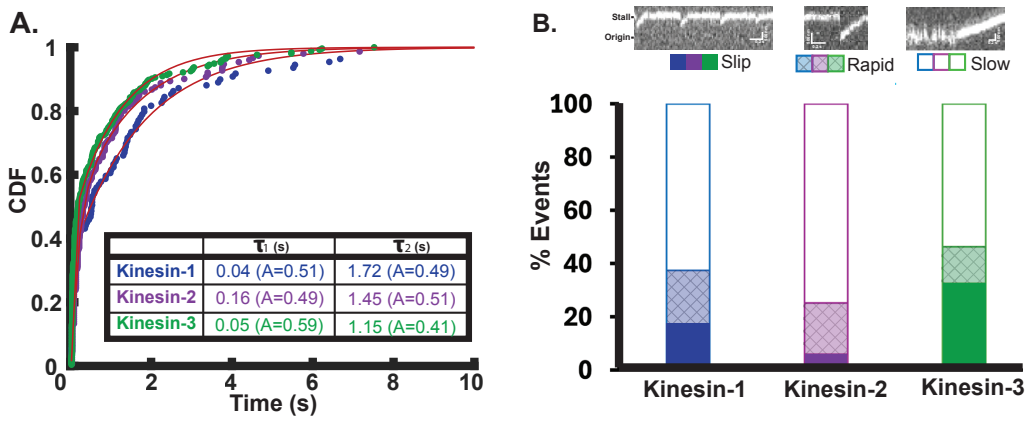

Figure 4. Reattachment Rates for Kinesin-1, -2 and -3. (A) Cumulative distribution of reattachment times for each motor fit to a bi-exponential by least squares. Kinesin-1 (blue) has a fast reattachment time constant of 0.04 s (95% CI [0.03, 0.04]), and a slow time constant of 1.72 s [1.65, 1.79] with (N=109 events). Kinesin-2 (purple) has a fast reattachment time constant of 0.16 s [0.15, 0.18], and a slow time constant of 1.45 s [1.34, 1.56] (N=151). Kinesin-3 (green) has a fast reattachment time constant of 0.05 s [0.04, 0.05]), and a slow time constant of 1.15 s [1.10, 1.20] (N=254). (B) Bar plot showing the fraction of slip, fast, and slow rebinding events for each motor, with example kymographs for each (top). Solid bars indicate slips during stall, where the motor resumes a new ramp within a single frame (~40 ms). Crosshatched shading indicates rapid reattachment events, where the motor falls back to within 400 nm of origin and initiates a new ramp within 100 ms. Open bars indicate slow reattachment events where motors detach from ramp or stall and fluctuate around the origin for >100 ms before rebinding and initiating a new ramp.

Simulating Potential Catch-Bond Mechanisms

To test potential mechanochemical mechanisms underlying the catch-bond behavior of the three kinesin motor families, we carried out stochastic simulations of

load-dependent motor stepping and detachment. For simplicity, we reduced the chemomechanical cycle down to a single strong-binding state (ATP and nucleotide-free states) and a single weak-binding state (ADP and ADP-Pi states). The three rate constants in this model are the strong-to-weak transition, $k_{s\text{-}w}$, the weak-to-strong transition, $k_{w\text{-}s}$, and a detachment rate from the weak-binding state, k_{det} (Figure 5A). Based on backstepping rates observed in optical tweezer experiments, we also incorporated a load-independent backward stepping rate of 3 s^{-1}, meaning that stall is defined as the load at which forward stepping slows to 3 s^{-1} (Andreasson, Shastry, et al., 2015; Carter & Cross, 2005; Coppin et al., 1997). For simplicity, we set $k_{s\text{-}w} = k_{w\text{-}s}$, meaning that the motor spends half of its cycle in each state in unloaded condition, and we set k_{det} to match the unloaded run duration (Figure 5B and Figure S7B).

Recent work provides strong evidence that the strong-to-weak transition is the load-dependent step in the kinesin-1 mechanochemical cycle (Sudhakar et al., 2021). Sudhakar et al synthesized germanium nanospheres that, due to their high index of refraction, enabled high trapping forces with particle diameters down to 70 nm. The faster response time due to the reduced drag coefficients resolved the 8 nm steps normally observed when motors are labeled through their tail domain into two ~4 nm substeps (Sudhakar et al., 2021). The duration of the first substep was increased both at low ATP and at elevated loads, whereas the second substep was unaffected by ATP or load and was the step from which motor detachments and backward slipping events occurred. These results map well to our two-state model; the strong-to-weak transition is both ATP and load-dependent (and likely involves neck linker docking), and the weak-to-strong transition (involving tethered head attachment to the next binding site) is load-independent.

We implemented these results into our two-state model for kinesin-1 by incorporating an exponential load-dependence into the strong-to-weak transition, such that the motor spends a greater fraction of its cycle in the strong-binding state at elevated loads. However, simulations from this $k_{s\text{-}w}(F)$ model predicted stall durations 10-fold longer than our measured kinesin-1 stall durations (Figure 5C). Thus, to match the experimental stall duration, we introduced an exponential load-dependence into the detachment rate, k_{det} (Figure 5B and Figure S7B). This model recapitulated both the unloaded run duration and the stall duration (Figure 5C), as well as generating a force-velocity curve that qualitatively matches our experiments (Figure S7C). Importantly, this model generates a catch-bond behavior without requiring a protein-protein interaction with a dissociation rate that decreases with load (Thomas et al., 2008). Instead, detachment from the weak-binding state is a slip bond (the dissociation rate increases with load), but by shifting the fraction of the cycle the motor spends in this vulnerable state, a catch-bond behavior is achieved. We also explored other model formulations, and formulated models to account for the kinesin-2 and -3 behavior, described in Supplementary Information (Figure S7E-S7H).

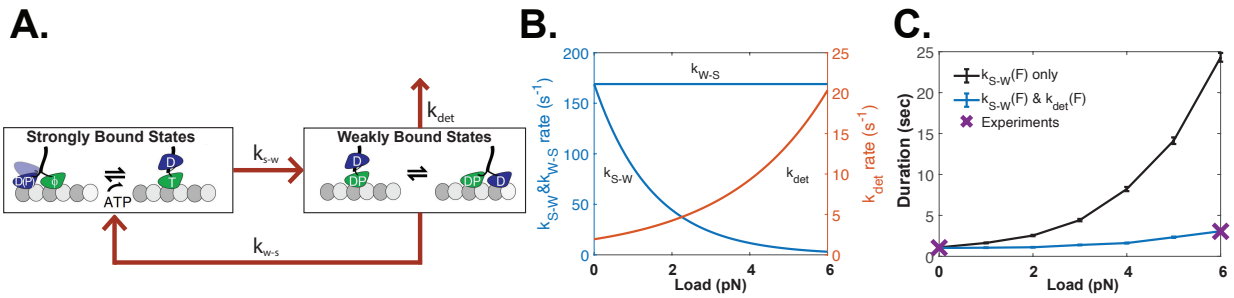

Figure 5. Chemomechanical Model of Possible Catch-bond Mechanism. (A) Diagram of kinesin chemomechanical cycle model consisting of a strong-binding state, a weak-binding state, and first-order rate constants for the strong-to-weak transition (k_{s-w}), the weak-to-strong transition (k_{w-s}), and detachment from the weak-binding state (k_{det}). (B) Load-dependent rate constants used to fit the experimental catch-bond behavior for kinesin-1. In this model the strong-to-weak transition (blue curve) slows with load and the detachment rate (red curve) increases with load, while the weak-to-strong transition (blue horizontal line) is independent of load. Model parameters are given in Table S4. (C) Experimental and simulated load-dependent off-rate for kinesin-1. Purple X show the experimental unloaded and stall durations for kinesin-1. Black line shows model in which only the strong-to-weak transition is load-dependent, showing that this model overestimates the stall duration. Blue line shows model using rate constants in (B), where a load-dependent k_{s-w} and k_{det} can recapitulate the experimental stall duration for kinesin-1. Simulations for kinesin-2 and -3 and results from other formulations of the model are presented in Figures S7-S10.

Discussion

Understanding how motors behave under physiologically relevant loads is crucial to understanding bidirectional transport in cells where cargo are transported by antagonistic kinesin and dynein motors (Cason & Holzbaur, 2022; Hancock, 2014). Optical tweezer experiments have provided many essential details of the kinesin mechanochemical cycle under load; however, the bead diameters needed to achieve substantial trapping forces impose vertical forces on the motors, complicating the interpretation of load-dependent off-rate measurements. Using DNA as a nanospring enables motor protein mechanical experiments using a standard TIRF microscope, which allows for simultaneous monitoring of numerous motor-DNA complexes in a single imaging field (Iwaki et al., 2016; Nick Maleki et al., 2023). In the geometry developed here, a kinesin motor pulls against the elastic force of a stretched DNA solely in a direction parallel to the microtubule, matching the geometry of vesicles measuring a few tens of nanometers. The most striking observation was that members of all three kinesin transport families show catch-bond behavior in which off-rates at stall are slower than those at low or zero loads. These findings necessitate a revised view of how kinesin motors operate against hindering loads and provide important constraints for uncovering the mechanisms that regulate bidirectional transport in cells.

Transport kinesins have a catch-bond behavior under hindering loads

Historically, motors have been studied with single bead assays in which motors are attached to a bead that is roughly 10-fold larger than the extended length of the motor (Andreasson, Shastry, et al., 2015; Block et al., 2003; Schnitzer et al., 2000; Valentine & Block, 2009). From these studies, motors from the kinesin-1, -2, and -3 families were all shown to have faster dissociation rates at increasing loads, with the

relative load-dependence kinesin-3 > kinesin-2 > kinesin-1 (Andreasson, Milic, et al., 2015; Andreasson, Shastry, et al., 2015; Budaitis et al., 2021; Kunwar et al., 2011; Pyrpassopoulos et al., 2023; Tomishige et al., 2002) . However, using a three-bead optical trap geometry, which minimizes vertical loads, it was found that kinesin-1 engagement times on the microtubule were longer lived than in the single-bead geometry (Pyrpassopoulos et al., 2020). We extend that result here to show that in our geometry, stall durations for kinesin-1 are roughly three-fold longer than unloaded run durations. Kinesin-2, which had previously been shown to detach much more readily under load than kinesin-1 in a single-bead force-clamp geometry (Andreasson, Shastry, et al., 2015), also had a stall duration that was 3-fold longer than the unloaded run duration. The kinesin-3 stall duration was within a factor of two of kinesin-1 and -2.

What is the mechanism of this catch-bond behavior? Cell adhesion proteins such as integrins, selectins, and FimH have been shown to form longer lasting bonds under load, with the proposed mechanisms generally involving an allosteric effect that strengthens the protein:protein interface (Kong et al., 2009; Marshall et al., 2003; Thomas et al., 2002). However, motor proteins are different in that they cycle in a nucleotide-dependent way between strong and weak binding states, offering multiple potential mechanisms for slower dissociation rates under load. For instance, under a few piconewtons of load, Myosin I was shown to dissociate nearly two orders of magnitude slower than in the absence of load, an effect attributed to load-dependent trapping of ADP in the active site that maintained the motor a high-affinity binding state (Laakso et al., 2008). Dynein was also shown to have catch-bond behavior over certain ranges of resisting loads, though the precise mechanism is unclear (Kunwar et al., 2011; Rai et al., 2016; Rai et al., 2013; Sanghavi et al., 2021). Using simulations of the kinesin chemomechanical cycle, we explored different potential mechanisms by which load can both slow the stepping rate and slow the dissociation rate at stall. The simplest modification, introducing load dependence into the strong-to-weak transition, actually predicted significantly longer stall durations than we measured experimentally (Figure 5C). The most straightforward model that could account for our results involved stall force loads slowing the strong-to-weak transition and accelerating the detachment rate from the weak-binding state.

Modeling the mechanochemical cycles enabled estimation of the load-dependence of the detachment rate from the weak-binding state for each motor. Using our modeling approach, where the load-dependent detachment rate $k_{det}(F) = k_{det}^{0} e^{\frac{F\delta}{k_B T}}$, we were able to recapitulate our kinesin-1 experimental results with a slip bond detachment distance parameter, denoting the relative sensitivity to load, of δ = 1.61 nm. The closest experimental comparison comes from kinesin-1 detachment experiments in ADP in which a motor-functionalized bead is dragged at constant velocity along an immobilized microtubule and binding/detachment events are detected by the bead stopping while trap continues to move (Andreasson, Shastry, et al., 2015; Uemura et al., 2002). Our distance parameter of 1.61 nm with an unloaded off-rate k_{det}^{0} of 1.93 s^{-1} falls between published values of 1 s^{-1} / 3 nm from Uemura et al and 11 s^{-1} / 0.4 nm from Andreasson et al. (Andreasson, Shastry, et al., 2015; Uemura et al., 2002).

Applying the two-state model to the other motors, we found that the load-dependent detachment kinetics of kinesin-2 and kinesin-3 were broadly similar to kinesin-1 (Figure S7E-H). This result was surprising given the strong load-dependence

of detachment for these motors seen in single-bead optical tweezer experiments (Andreasson, Shastry, et al., 2015; Uemura et al., 2002). Using the same model we used for interpreting kinesin-1, we found the load dependence of detachment from the weak-binding state was in the order kinesin-3 (2.14 nm) > kinesin-1 (1.6 nm) > kinesin-2 (1.35 nm) (Figure S7B).

The role of vertical forces in motor detachment

We next asked whether by considering the different geometries we could reconcile our catch-bond observations with previous single-bead optical tweezer kinesin-1 slip-bond measurements that found the kinesin-1 off-rate increased from 1.11 s^{-1} at zero load to 2.67 s^{-1} at 6 pN (reproduced in Figure S10) (Andreasson, Milic, et al., 2015; Andreasson, Shastry, et al., 2015). Previous modeling work accounted for these off-rates using a two-step detachment process having catch-bond behavior for parallel loads and slip-bond behavior for vertical loads (Khataee & Howard, 2019). Using our two-state model, we instead incorporated both horizontal and vertical loads as accelerating detachment from the weak-binding state:

$$k_{det}(F) = k_{det}^{0} e^{\frac{(F_{\parallel}\delta_{\parallel} + F_{\perp}\delta_{\perp})}{k_B T}}$$

Here $F_{\parallel}$ and $F_{\perp}$ are the magnitude of the parallel and perpendicular loads and $\delta_{\parallel}$ and $\delta_{\perp}$ represent the distance parameters in each direction (Figure S10B). Using a 440 nm bead diameter and estimated motor length of 35 nm that results in the force being imposed on the motor at a 60º angle (Figure S10A), it was calculated that a 6 pN force parallel to the microtubule would correspond to a 10 pN force perpendicular to the microtubule (Andreasson, Milic, et al., 2015; Andreasson, Shastry, et al., 2015; Khataee & Howard, 2019). Using $\delta_{\parallel}$ = 1.61 from our model in Figure 5, we found that by setting $\delta_{\perp}$ = 1.58 nm, we were able to reproduce the slip bond behavior observed in the single-bead optical trap experiments (Figure S10D). Notably, in this model the detachment rate from the weak-binding state has a slip bond character with similar load dependencies in the parallel and perpendicular directions. We stress that this model is a hypothesis that needs further testing, and that the load-dependent off-rate over intermediate loads does not match the experimental data (Figure S10D). Nonetheless, this is a simple formulation that shows that a motor can display either catch bond or slip bond behavior depending on the geometry of the imposed loads.

Ramps reveal detachment behaviors at low loads

In addition to reporting on the detachment properties at stall, our DNA tensiometer provides new insights into fast rebinding that occurs during unloaded runs of kinesin-3. It has long been appreciated that the kinesin-3 motor KIF1A achieves long run lengths due to electrostatic attraction between its positively charged Loop-12 (K-loop) and the negatively charged C-terminal tail of tubulin (Lessard et al., 2019; Okada et al., 2003; Okada & Hirokawa, 1999, 2000; Soppina et al., 2014; Soppina & Verhey, 2014; Zaniewski et al., 2020; Zaniewski & Hancock, 2023). Furthermore, the KIF1A off-rate in ADP, in which the motor diffuses on the microtubule lattice, was found to match the off-rate during processive stepping in ATP (Zaniewski et al., 2020). The relatively high microtubule affinity of this weak-binding state suggests that the motor may be

undergoing diffusive episodes between processive runs, while maintaining association with the microtubule. In this way, the observed run length would be a concatenation of a number of shorter runs interspersed by diffusive events.

Our DNA tensiometer offers a way to test the hypothesis that the long, unloaded run lengths of KIF1A are due to a concatenation of shorter runs. Due to the nonlinearity of the dsDNA force-extension curve in our DNA tensiometer, the motor is walking against forces below 1 pN for roughly 90% of the distance to stall (Figure 1B). Consistent with this, motor velocities were nearly constant until they were near the stall force (Figure 1D and S3), and ramp velocities averaged only ~15% slower than unloaded velocities (Table S3), which corresponds to ~1 pN of force if the force-velocity relationship is linear. By developing a Markov Process/Bayesian Inference approach to estimate the KIF1A detachment rate during ramps, we were able to estimate the run duration at low loads. Importantly, this analysis takes into account both motors that dissociate during the ramps and those that complete ramps by achieving stall. We found that the KIF1A ramp duration parameter was nearly four-fold shorter than the unloaded run duration parameter (Figure 3). If, under zero load, the long runs observed were actually a concatenation of a series of shorter runs connected by diffusive weak-binding events, the diffusive state would likely be unable to withstand even the sub-pN forces from the DNA spring (Okada & Hirokawa, 2000). For instance, based on a 0.044 $\mu m^2/s$ diffusion coefficient (equivalent to a ~0.1 pN-s/μm drag coefficient (Howard, 2001; Okada & Hirokawa, 2000)), if the motor were in a weak-binding state for 10 ms, a 1 pN force would pull the motor back 100 nm. Thus, in considering whether KIF1A acts as a catch bond, we used this ramp duration as the best approximation for the true run unloaded length in the absence of diffusive events. The electrostatic interactions that enable KIF1A to be superprocessive do not only act during each step to enhance the probability of completing the step; they also act between runs to maintain association of KIF1A with the microtubule, enabling rebinding and initiation of new runs.

The ramp durations of kinesin-1 and kinesin-2 also provide insights into how load alters their interactions with microtubules. For kinesin-2, the predicted ramp duration was not statistically different from the unloaded run duration, suggesting that unloaded runs do not include short diffusive episodes. This result is somewhat surprising, given previous kinesin-2 force-clamp optical tweezer experiments that found a substantial drop in run length between the unloaded case and the lowest force (1 pN) and a smooth reduction in run length at higher forces ((Andreasson, Shastry, et al., 2015); Figure 4A). However, this discrepancy may be due to vertical forces associated with the single bead geometry accelerating the detachment rate in the optical tweezer study (Khataee & Howard, 2019). Interestingly the predicted ramp duration for kinesin-1 was nearly the same as the stall duration and much longer than the unloaded duration. One possibility for this puzzling result is that the catch-bond effect of hindering load comes into play at low loads and not only at stall where the motor has slowed considerably.

Motor slips and detachments reflect different processes

Because the DNA tensiometer tethers the motor near the microtubule, such that repeated binding and unbinding events occur, it enables comparison of family-dependent differences in kinesin rebinding kinetics. Kinesin-microtubule interactions can be separated into three classes: i) the initial binding from solution, ii) motor

rebinding following an attachment/detachment event, and iii) fast motor rebinding seen in slip events during ramps and at stall. Previous stopped-flow studies on these three motors in the same buffer used here found that the solution bi-molecular on-rates were 1.1 $\mu M^{-1}s^{-1}$ for kinesin-1, 3.1 $\mu M^{-1}s^{-1}$ for kinesin-2, and 17 $\mu M^{-1}s^{-1}$ for kinesin-3 (Chen et al., 2015; Feng et al., 2018; Zaniewski et al., 2020). We observed two classes of detachments during stall plateaus, full detachments and slips. Detachment events, which we defined as the motor returning to within 400 nm of the baseline, could be separated into fast events, when a new ramp started within the limit of detection (typically ~0.04 s), and slower events where the motor fluctuated around the origin for multiple seconds. When we fit a bi-exponential to the distribution of all slip and detachment events, the slow phases ranged from 1.72 s for kinesin-3 down to 1.15 s for kinesin-1. Thus, although there were differences between motors, the large variation expected from the stopped-flow studies was not manifested in the slow reattachment durations. Our tentative interpretation is that either the hydrodynamic drag of the DNA and Qdot or the negative charge of the DNA limits the motor on-rate, masking any family-dependent differences.

Slip events were observed for all three motors, with highest frequency for kinesin-3 and lowest frequency for kinesin-1. These slips were first characterized in a 2019 kinesin-1 optical tweezer study from the Cross lab (Toleikis et al., 2020), where at stall, backward displacements could be observed at multiples of 8 nm that were distinct from detachment events. The durations of the plateaus that preceded the slips were longer than the plateaus preceding forward steps, suggesting that the motor transitioned into a different state preceding the slip, such as phosphate dissociation to generate the ADP state. Subsequent higher resolution work, enabled by small Germanium nanoparticles, revealed a staircase pattern during these slips with ~8 nm steps of mean duration 73 μsec, suggesting that the motor was transiently interacting with each tubulin subunit as it slipped backward. Similar slips had been seen earlier for kinesin-2 (Andreasson, Shastry, et al., 2015), and were subsequently seen for two kinesin-3 family members, KIF1A and KIF1C (Pyrpassopoulos et al., 2023; Siddiqui et al., 2022). Using a three-bead optical tweezer geometry, it was found that for KIF1A, ~80% of slip/detachment events lasted less than 10 ms before the motor started a new ramp, whereas for kinesin-1 only ~25% of the slip/detachment events were 10 ms or shorter.

We found that kinesin-3 had roughly twice as many slips as kinesin-1 (Figure 4B). We also found that in the bi-exponential fit to the slip/detachment durations, 34% of the kinesin-1 events were in the fast population, compared to 44% and 46% for kinesin-2 and kinesin-3, respectively. With regard to the catch-bond behavior at stall, perhaps the most informative way to analyze the influence of slips is to compare the stall durations for the three motors when the slip events at stall are ignored. This approach is relevant to tug-of-war events in cells because when kinesin fully detaches, dynein would be able to walk unimpeded until kinesin rebinds; in contrast, kinesin slip events would only lead to a transient elastic recoil of the cargo before the motor regained a footing and continued pulling against dynein. Ignoring slips lead to a 1.5-fold increase in the stall duration for kinesin-1 to 4.4 s, a 2.4-fold increase for kinesin-2 to 6.8 s, and a 3.0-fold increase for kinesin-3 to 5.6 s (Figure S4 and Table S2).

Catch-bond behavior provides insights into tug-of-war with dynein

Consistent with the diversity of intracellular cargo transported by kinesin and dynein, there are many features such as motor number and type, microtubule isotype, and cargo size and geometry that can regulate transport. In previous simulations of kinesin-dynein tug-of-war transport, we found that the strongest determinants of kinesin's ability to compete against dynein were the load-dependent motor dissociation rate and the motor rebinding rate (Ma et al., 2023; Ohashi et al., 2019). Simply put, if motors detach, then the opposing motor wins, and if they remain attached against strong antagonistic loads, they can at least achieve a stalemate against their opposition. The finding here that all three dominant kinesin transport families display catch-bond behavior at stall necessitates a reevaluation of how motors function during a tug-of-war. There is evidence that dynein forms a catch bond or at least an ideal (load independent) bond (Belyy et al., 2016; Cianfrocco et al., 2015; Kunwar et al., 2011; Rai et al., 2016; Rai et al., 2013; Sanghavi et al., 2021); thus, kinesins and dyneins are primed to strongly oppose on another. Consistent with this, when vesicle motility is quantified during axonal transport, there are often a large fraction of immobile vesicles and even those that move include sustained immobile episodes (Encalada et al., 2011; Fu & Holzbaur, 2013; Gross et al., 2002; Hancock, 2014; Iacobucci et al., 2014). It's possible that no motors are engaged in these cases, but it's also possible that the motors are stalled in a tug-of-war with the large antagonistic forces suppressing the kinesin and dynein off-rates.

The catch bond results here help to explain previous in vitro work in which one kinesin and one dynein were connected through a complementary ssDNA (Belyy et al., 2016; Feng et al., 2020; Gicking et al., 2022). It was found that the motor pairs had periods of near-zero velocity that lasted for many seconds, considerably longer than kinesin's unloaded off-rate. Furthermore, kinesin-2 and kinesin-3 also showed these sustained slow tug-of-war periods despite their reported faster load-dependent off-rates from optical tweezer studies. The functional catch-bond behavior observed here provides a simple explanation for these sustained kinesin-dynein stalemates.

Importantly, the load-dependent off-rates of both kinesins and dynein are expected to depend on the cargo geometry. A 30 nm vesicle would lead to forces on the motor nearly parallel to the microtubule surface, whereas when transporting a micron-scale mitochondria the vertical forces would be larger than the horizontal forces. Cargo geometry and stiffness is also expected to play a role; for instance, deformation of a cargo, either due to compliance of the cargo or to multiple motors pulling on it will tend to reduce vertical force components on the motors. The present work emphasizes that along with motor type, motor number, motor autoinhibition, and the growing list of regulatory proteins, the geometry with kinesin and dynein engage in a tug-of-war can be an important determinant of the speed and direction of cargo transport in cells.

Methods

DNA Tensiometer Construction

For the dsDNA spring, a 5' biotinylated forward primer (5'-/5Biosg/TGC CTC CGT GTA AGG GGG AT-3') and a reverse primer with a 5' overhang (5'-/GGG CCA TCG CCA ATT GGA GTA /idSp/ GTG AGT TAA AGT TGT ACT CGA GTT TGT GTC CAA GAA -3') were used to create a 3009 bp dsDNA by PCR from plasmid *Mus Musculus* BicD2-

sf-GFP (aa 25-425) in pet28a. The abasic Int 1',2'-Dideoxyribose spacer (idSp) creates an overhang by terminating the polymerase. All oligonucleotides were purchased from IDT. Each 50 μL PCR reaction contained: 1x Phusion HF buffer, 198 μM dNTPs, 2 μM dCTP-Cy5, 0.5 μM primers, 3 ng template DNA and 1 U/50 μL HF Phusion Polymerase. Fluorescent dsDNA used in Figure S5 had 10μM dCTP-Cy5 and 190μM dNTPs. The PCR reaction was carried out in a thermal cycler with the following procedure: 98℃ for 30 s, then 45 cycles of 98℃ for 10 s, 58℃ for 30 s and 72℃ for 1.5 min, then lastly 72℃ for 5 min. The product was purified using a NucleoSpin® PCR clean-up kit and the concentration determined by absorbance on a Nanodrop 2000c Spectrophotometer. DNA bands were visualized on a 1% agarose gel with ethidium bromide staining.

Motor-Microtubule-Tensiometer Assembly

Motors were bacterially expressed, purified and linked through its SNAP tag to an oligonucleotide (5'-/TAC TCC AAT TGG CGA TGG CCC / 3AmMC6T/-3') complementary to the dsDNA overhang. Details of motor expression, purification and labeling, as well as tubulin biotinylation and polymerization are given in Supplementary Information. The DNA tensiometer was assembled on the microtubule as follows. The following three buffers are made on the same day of the experiment: C2AT (BRB80, 10 μM Taxol, 2 mM MgATP, 2 mg/mL Casein), 2AT (BRB80, 10 μM Taxol, 2 mM MgATP) and Imaging Solution (BRB80, 10 μM Taxol, 2 mg/mL Casein, 2 mM MgATP, 20 mM D-glucose, 0.02 mg/mL Glucose oxidase, 0.008 mg/mL Catalase, 0.5% BME and 2 mg/mL BSA). Full-length rigor kinesin was used to attach microtubules the coverglass (Mickolajczyk et al., 2015). Tensiometers were created in the flow cell using the following work flow: C2AT, 5 min > Rigor kinesin, 5 min> C2AT wash > BioMT, 5 min > 2AT > 8 nM Neutravidin, 5 min> 2AT > 10 nM Bio-dsDNA-Overhang, 5 min> C2AT > 4 nM KinesinMotor + 40nM Qdot-GBP (pre incubated in tube on ice for >15 min) in imaging solution, 10 min > Imaging solution wash. Note that because casein can contain free biotin, casein-free 2AT buffer was used during avidin-biotin binding steps. Following assembly, the Qdot connected to the motor was imaged on a custom-built TIRF microscope, described previously (Nong et al., 2021). Raw data were typically collected at 25 fps (range of 20-40 fps) on a Photometrics Prime 95B camera.

Data Analysis

Movies were uploaded into FIESTA software (Ruhnow et al., 2011) and Qdot intensities were tracked using a symmetric 2-D gaussian function to obtain x,y,t data for each Qdot. When drift correction was needed, TetraSpeck™ Fluorescent Microspheres (Thermo) and immobile Qdots were used as fiducial markers. The smallest position errors at stall in FIESTA fitting were 3-4 nm, which matched the positional error of Qdot-labeled motors stuck to microtubules in AMPPNP. Points with position errors greater than 20 nm were excluded because they often involved clearly spurrious position estimates. Notably, many tensiometers had small segments of missing data due to the Qdot fluctuating out of the TIRF field or blinking; these occurred most often during periods when the motors were detached from the microtubule.

After obtaining X and Y positions of linear motor tracks in Fiesta, we rotated and translated the data in Excel to generate X versus t traces. The apparent origin was determined by averaging the points where the motor is fluctuating on its tether. In rare

instances where no fluctuation was observed, the approximate origin was calculated by averaging the starting positions of all the ramps within the tensiometer (Figure 1). We then measured the ramp time, distance traveled, stall durations, reattachment times and starting positions. Tensiometers occasionally ended with the Qdot signal going dark, denoting either bleaching or failure of the Qdot-motor or motor-DNA connection. Notably, no clear instances of motor-Qdots detaching during stall and continuing walking (denoting the tensiometer breaking) were observed. Stalls that terminated due to the tensiometer going dark or the video ending were excluded from analysis.

Stochastic Modeling

Kinesin run and stall durations were simulated by using a modified version of published stochastic model of kinesin stepping (Gicking et al., 2022; Ma et al., 2023). A motor is either in a strongly-bound state or a weakly-bound state (Figure 5A). At each timepoint, a motor in the strongly bound state can step backward by 8 nm with a constant rate, $k_{back} = 3\ s^{-1}$, or transition into the weakly bound state with a first order transition rate constant, k_{S-W}. A motor in the weakly bound state can complete an 8-nm forward step by transitioning back to the strongly-bound state with rate constant, k_{W-S}, or it can detach from the microtubule with transition rate, k_{det}. All of these transitions are irreversible. The model can be solved analytically. The forward stepping rate and the load-dependent velocity are:

$$k_{forward} = \left(\frac{1}{k_{S-W}} + \frac{1}{k_{W-S}}\right)^{-1}$$

$$V(F) = 8\ nm * (k_{forward} - k_{back})$$

Ignoring relatively slow backstepping rate in stepping cycle, the bound duration is equal to the duration of each step multiplied by the predicted number of steps before detaching:

$$T(F) = \left(\frac{1}{k_{S-W}} + \frac{1}{k_{W-S}}\right)^{-1} * \left(\frac{k_{W-S} + k_{det}}{k_{W-S}}\right)$$

For simplicity, we set $k_{S-W} = k_{W-S}$ at zero load. Load-dependent transition rates were defined as follows,

$$k(F) = k^0 * e^{\frac{F\delta}{k_B T}}$$

where k^0 is the unloaded transition rate, δ is the characteristic distance parameter and $k_B T$ is the Boltzmann's constant multiplied by the absolute temperature, equal to 4.1 pN-nm at $25°$ C. The forward stepping rates for unloaded kinesin-1, -2, -3 simulation were set to 84.5, 53 and 151.5 steps per second, respectively, and set to 3 s^{-1} (matching the backstepping rate) at the stall force, defined as 6 pN. All simulations were run 1000 times, and each run started from a motor in strongly bound state and continued until detachment or until 50 seconds. The durations of all the runs were averaged and plotted with standard error of mean (SEM).

Acknowledgments

This work was originally conceived as part of a NIH-funded collaborative modeling project to Will Hancock, Scott McKinley, John Fricks, and Peter Kramer

(R01GM122082). We thank Qingzhou Feng, Scott Pflumm, and Adheshwari Ramesh for early efforts on this project and all members of the Hancock Lab for helpful discussions. This work was funded by NIH Grant R35GM139568 to W.O.H.. C.R.N. was supported by NIH postdoctoral fellowship F32GM149114, R.J. was supported by NIH Training Grant T32GM108563, and S.A.M. was supported by the NSF-Simons Southeast Center for Mathematics and Biology (SCMB) through grant NSF-DMS1764406 and Simons Foundation-SFARI 594594.

References

Andreasson, J. O., Milic, B., Chen, G. Y., Guydosh, N. R., Hancock, W. O., & Block, S. M. (2015). Examining kinesin processivity within a general gating framework. *Elife*, *4*. https://doi.org/10.7554/eLife.07403

Andreasson, J. O., Shastry, S., Hancock, W. O., & Block, S. M. (2015). The Mechanochemical Cycle of Mammalian Kinesin-2 KIF3A/B under Load. *Curr Biol*, *25*(9), 1166-1175. https://doi.org/10.1016/j.cub.2015.03.013

Bell, G. I. (1978). Models for the specific adhesion of cells to cells. *Science*, *200*(4342), 618-627. https://doi.org/10.1126/science.347575

Belyy, V., Schlager, M. A., Foster, H., Reimer, A. E., Carter, A. P., & Yildiz, A. (2016). The mammalian dynein-dynactin complex is a strong opponent to kinesin in a tug-of-war competition. *Nat Cell Biol*, *18*(9), 1018-1024. https://doi.org/10.1038/ncb3393

Bilsland, L. G., Sahai, E., Kelly, G., Golding, M., Greensmith, L., & Schiavo, G. (2010). Deficits in axonal transport precede ALS symptoms in vivo. *Proc Natl Acad Sci U S A*, *107*(47), 20523-20528. https://doi.org/10.1073/pnas.1006869107

Blehm, B. H., Schroer, T. A., Trybus, K. M., Chemla, Y. R., & Selvin, P. R. (2013). In vivo optical trapping indicates kinesin's stall force is reduced by dynein during intracellular transport. *Proc Natl Acad Sci U S A*, *110*(9), 3381-3386. https://doi.org/10.1073/pnas.1219961110

Block, S. M., Asbury, C. L., Shaevitz, J. W., & Lang, M. J. (2003). Probing the kinesin reaction cycle with a 2D optical force clamp. *Proc Natl Acad Sci U S A*, *100*(5), 2351-2356. https://doi.org/10.1073/pnas.0436709100

Brenner, D., Yilmaz, R., Muller, K., Grehl, T., Petri, S., Meyer, T., Grosskreutz, J., Weydt, P., Ruf, W., Neuwirth, C., Weber, M., Pinto, S., Claeys, K. G., Schrank, B., Jordan, B., Knehr, A., Gunther, K., Hubers, A., Zeller, D.,…German, A. L. S. n. M. N. D. N. E. T. (2018). Hot-spot KIF5A mutations cause familial ALS. *Brain*, *141*(3), 688-697. https://doi.org/10.1093/brain/awx370

Budaitis, B. G., Jariwala, S., Rao, L., Yue, Y., Sept, D., Verhey, K. J., & Gennerich, A. (2021). Pathogenic mutations in the kinesin-3 motor KIF1A diminish force generation and movement through allosteric mechanisms. *J Cell Biol*, *220*(4). https://doi.org/10.1083/jcb.202004227

Caballero Oteyza, A., Battaloglu, E., Ocek, L., Lindig, T., Reichbauer, J., Rebelo, A. P., Gonzalez, M. A., Zorlu, Y., Ozes, B., Timmann, D., Bender, B., Woehlke, G., Zuchner, S., Schols, L., & Schule, R. (2014). Motor protein mutations cause a new form of hereditary spastic paraplegia. *Neurology*, *82*(22), 2007-2016. https://doi.org/10.1212/WNL.0000000000000479

Carter, N. J., & Cross, R. A. (2005). Mechanics of the kinesin step. *Nature*, *435*(7040), 308-312. https://doi.org/10.1038/nature03528

Cason, S. E., & Holzbaur, E. L. F. (2022). Selective motor activation in organelle transport along axons. *Nat Rev Mol Cell Biol*, *23*(11), 699-714. https://doi.org/10.1038/s41580-022-00491-w

Chen, G. Y., Arginteanu, D. F., & Hancock, W. O. (2015). Processivity of the kinesin-2 KIF3A results from rear head gating and not front head gating. *J Biol Chem*, *290*(16), 10274-10294. https://doi.org/10.1074/jbc.M114.628032

Cianfrocco, M. A., DeSantis, M. E., Leschziner, A. E., & Reck-Peterson, S. L. (2015). Mechanism and regulation of cytoplasmic dynein. *Annu Rev Cell Dev Biol*, *31*, 83-108. https://doi.org/10.1146/annurev-cellbio-100814-125438

Coppin, C. M., Pierce, D. W., Hsu, L., & Vale, R. D. (1997). The load dependence of kinesin's mechanical cycle. *Proc Natl Acad Sci U S A*, *94*(16), 8539-8544. https://doi.org/10.1073/pnas.94.16.8539

Encalada, S. E., Szpankowski, L., Xia, C. H., & Goldstein, L. S. (2011). Stable kinesin and dynein assemblies drive the axonal transport of mammalian prion protein vesicles. *Cell*, *144*(4), 551-565. https://doi.org/10.1016/j.cell.2011.01.021

Ezber, Y., Belyy, V., Can, S., & Yildiz, A. (2020). Dynein Harnesses Active Fluctuations of Microtubules for Faster Movement. *Nat Phys*, *16*, 312-316. https://doi.org/10.1038/s41567-019-0757-4

Feng, Q., Gicking, A. M., & Hancock, W. O. (2020). Dynactin p150 promotes processive motility of DDB complexes by minimizing diffusional behavior of dynein. *Mol Biol Cell*, *31*(8), 782-792. https://doi.org/10.1091/mbc.E19-09-0495

Feng, Q., Mickolajczyk, K. J., Chen, G. Y., & Hancock, W. O. (2018). Motor Reattachment Kinetics Play a Dominant Role in Multimotor-Driven Cargo Transport. *Biophys J*, *114*(2), 400-409. https://doi.org/10.1016/j.bpj.2017.11.016

Fu, M. M., & Holzbaur, E. L. (2013). JIP1 regulates the directionality of APP axonal transport by coordinating kinesin and dynein motors. *J Cell Biol*, *202*(3), 495-508. https://doi.org/10.1083/jcb.201302078

Gicking, A. M., Ma, T. C., Feng, Q., Jiang, R., Badieyan, S., Cianfrocco, M. A., & Hancock, W. O. (2022). Kinesin-1, -2, and -3 motors use family-specific mechanochemical strategies to effectively compete with dynein during bidirectional transport. *Elife*, *11*. https://doi.org/10.7554/eLife.82228

Gross, S. P. (2004). Hither and yon: a review of bi-directional microtubule-based transport. *Phys Biol*, *1*(1-2), R1-11. https://doi.org/10.1088/1478-3967/1/2/R01

Gross, S. P., Welte, M. A., Block, S. M., & Wieschaus, E. F. (2002). Coordination of opposite-polarity microtubule motors. *J Cell Biol*, *156*(4), 715-724. https://doi.org/10.1083/jcb.200109047

Hancock, W. O. (2014). Bidirectional cargo transport: moving beyond tug of war. *Nat Rev Mol Cell Biol*, *15*(9), 615-628. https://doi.org/10.1038/nrm3853

Hendricks, A. G., Perlson, E., Ross, J. L., Schroeder, H. W., 3rd, Tokito, M., & Holzbaur, E. L. (2010). Motor coordination via a tug-of-war mechanism drives bidirectional vesicle transport. *Curr Biol*, *20*(8), 697-702. https://doi.org/10.1016/j.cub.2010.02.058

Howard, J. (2001). *Mechanics of Motor Proteins and the Cytoskeleton*. Sinauer Associates.

Howard, J., & Hancock, W. O. (2020). Three Beads Are Better Than One. *Biophys J*, *118*(1), 1-3. https://doi.org/10.1016/j.bpj.2019.12.001

Iacobucci, G. J., Rahman, N. A., Valtuena, A. A., Nayak, T. K., & Gunawardena, S. (2014). Spatial and temporal characteristics of normal and perturbed vesicle transport. *PLoS One*, *9*(5), e97237. https://doi.org/10.1371/journal.pone.0097237

Iwaki, M., Wickham, S. F., Ikezaki, K., Yanagida, T., & Shih, W. M. (2016). A programmable DNA origami nanospring that reveals force-induced adjacent binding of myosin VI heads. *Nat Commun*, *7*, 13715. https://doi.org/10.1038/ncomms13715

Khataee, H., & Howard, J. (2019). Force Generated by Two Kinesin Motors Depends on the Load Direction and Intermolecular Coupling. *Phys Rev Lett*, *122*(18), 188101. https://doi.org/10.1103/PhysRevLett.122.188101

Kojima, H., Muto, E., Higuchi, H., & Yanagida, T. (1997). Mechanics of single kinesin molecules measured by optical trapping nanometry. *Biophys J*, *73*(4), 2012-2022. https://doi.org/10.1016/S0006-3495(97)78231-6

Kong, F., Garcia, A. J., Mould, A. P., Humphries, M. J., & Zhu, C. (2009). Demonstration of catch bonds between an integrin and its ligand. *J Cell Biol*, *185*(7), 1275-1284. https://doi.org/10.1083/jcb.200810002

Kunwar, A., Tripathy, S. K., Xu, J., Mattson, M. K., Anand, P., Sigua, R., Vershinin, M., McKenney, R. J., Yu, C. C., Mogilner, A., & Gross, S. P. (2011). Mechanical stochastic tug-of-war models cannot explain bidirectional lipid-droplet transport. *Proc Natl Acad Sci U S A*, *108*(47), 18960-18965. https://doi.org/10.1073/pnas.1107841108

Laakso, J. M., Lewis, J. H., Shuman, H., & Ostap, E. M. (2008). Myosin I can act as a molecular force sensor. *Science*, *321*(5885), 133-136. https://doi.org/10.1126/science.1159419

Lessard, D. V., Zinder, O. J., Hotta, T., Verhey, K. J., Ohi, R., & Berger, C. L. (2019). Polyglutamylation of tubulin's C-terminal tail controls pausing and motility of kinesin-3 family member KIF1A. *J Biol Chem*, *294*(16), 6353-6363. https://doi.org/10.1074/jbc.RA118.005765

Ma, T. C., Gicking, A. M., Feng, Q., & Hancock, W. O. (2023). Simulations suggest robust microtubule attachment of kinesin and dynein in antagonistic pairs. *Biophys J*, *122*(16), 3299-3313. https://doi.org/10.1016/j.bpj.2023.07.007

Makrythanasis, P., Maroofian, R., Stray-Pedersen, A., Musaev, D., Zaki, M. S., Mahmoud, I. G., Selim, L., Elbadawy, A., Jhangiani, S. N., Coban Akdemir, Z. H., Gambin, T., Sorte, H. S., Heiberg, A., McEvoy-Venneri, J., James, K. N., Stanley, V., Belandres, D., Guipponi, M., Santoni, F. A.,…Antonarakis, S. E. (2018). Biallelic variants in KIF14 cause intellectual disability with microcephaly. *Eur J Hum Genet*, *26*(3), 330-339. https://doi.org/10.1038/s41431-017-0088-9

Marko, J. F., & Siggia, E. D. (1995). Stretching DNA. *Macromolecules*, *28*(26), 8759-8770. https://siggia.rockefeller.edu/Publications/1990-9_files/markoMacromol1995.pdf

Marshall, B. T., Long, M., Piper, J. W., Yago, T., McEver, R. P., & Zhu, C. (2003). Direct observation of catch bonds involving cell-adhesion molecules. *Nature*, *423*(6936), 190-193. https://doi.org/10.1038/nature01605

Martin, M., Iyadurai, S. J., Gassman, A., Gindhart, J. G., Jr., Hays, T. S., & Saxton, W. M. (1999). Cytoplasmic dynein, the dynactin complex, and kinesin are interdependent and essential for fast axonal transport. *Mol Biol Cell*, *10*(11), 3717-3728. https://doi.org/10.1091/mbc.10.11.3717

Mickolajczyk, K. J., Deffenbaugh, N. C., Arroyo, J. O., Andrecka, J., Kukura, P., & Hancock, W. O. (2015). Kinetics of nucleotide-dependent structural transitions in the kinesin-1 hydrolysis cycle. *Proc Natl Acad Sci U S A*, *112*(52), E7186-7193. https://doi.org/10.1073/pnas.1517638112

Millecamps, S., & Julien, J. P. (2013). Axonal transport deficits and neurodegenerative diseases. *Nat Rev Neurosci*, *14*(3), 161-176. https://doi.org/10.1038/nrn3380

Moawia, A., Shaheen, R., Rasool, S., Waseem, S. S., Ewida, N., Budde, B., Kawalia, A., Motameny, S., Khan, K., Fatima, A., Jameel, M., Ullah, F., Akram, T., Ali, Z., Abdullah, U., Irshad, S., Hohne, W., Noegel, A. A., Al-Owain, M.,…Hussain, M. S. (2017). Mutations of KIF14 cause primary microcephaly by impairing cytokinesis. *Ann Neurol*, *82*(4), 562-577. https://doi.org/10.1002/ana.25044

Muller, M. J., Klumpp, S., & Lipowsky, R. (2008). Tug-of-war as a cooperative mechanism for bidirectional cargo transport by molecular motors. *Proc Natl Acad Sci U S A*, *105*(12), 4609-4614. https://doi.org/10.1073/pnas.0706825105

Nick Maleki, A., Huis In 't Veld, P. J., Akhmanova, A., Dogterom, M., & Volkov, V. A. (2023). Estimation of microtubule-generated forces using a DNA origami nanospring. *J Cell Sci*, *136*(5). https://doi.org/10.1242/jcs.260154

Nicolas, A., Kenna, K. P., Renton, A. E., Ticozzi, N., Faghri, F., Chia, R., Dominov, J. A., Kenna, B. J., Nalls, M. A., Keagle, P., Rivera, A. M., van Rheenen, W., Murphy, N. A., van Vugt, J., Geiger, J. T., Van der Spek, R. A., Pliner, H. A., Shankaracharya, Smith, B. N.,…Landers, J. E. (2018). Genome-wide Analyses Identify KIF5A as a Novel ALS Gene. *Neuron*, *97*(6), 1267-1288. https://doi.org/10.1016/j.neuron.2018.02.027

Nong, D., Haviland, Z. K., Kuntz, K. V., Tien, M., Anderson, C. T., & Hancock, W. O. (2021). Integrated multi-wavelength microscope combining TIRFM and IRM modalities for imaging cellulases and other processive enzymes. *Biomed Opt Express*, *12*(6), 3253-3264. https://doi.org/10.1364/BOE.423798

Ohashi, K. G., Han, L., Mentley, B., Wang, J., Fricks, J., & Hancock, W. O. (2019). Load-dependent detachment kinetics plays a key role in bidirectional cargo transport by kinesin and dynein. *Traffic*, *20*(4), 284-294. https://doi.org/10.1111/tra.12639

Okada, Y., Higuchi, H., & Hirokawa, N. (2003). Processivity of the single-headed kinesin KIF1A through biased binding to tubulin. *Nature*, *424*(6948), 574-577. https://doi.org/10.1038/nature01804

Okada, Y., & Hirokawa, N. (1999). A processive single-headed motor: kinesin superfamily protein KIF1A. *Science*, *283*(5405), 1152-1157. https://doi.org/10.1126/science.283.5405.1152

Okada, Y., & Hirokawa, N. (2000). Mechanism of the single-headed processivity: diffusional anchoring between the K-loop of kinesin and the C terminus of tubulin. *Proc Natl Acad Sci U S A*, *97*(2), 640-645. https://doi.org/10.1073/pnas.97.2.640

Pant, D. C., Parameswaran, J., Rao, L., Loss, I., Chilukuri, G., Parlato, R., Shi, L., Glass, J. D., Bassell, G. J., Koch, P., Yilmaz, R., Weishaupt, J. H., Gennerich, A.,

& Jiang, J. (2022). ALS-linked KIF5A DeltaExon27 mutant causes neuronal toxicity through gain-of-function. *EMBO Rep*, *23*(8), e54234. https://doi.org/10.15252/embr.202154234

Pyrpassopoulos, S., Gicking, A. M., Zaniewski, T. M., Hancock, W. O., & Ostap, E. M. (2023). KIF1A is kinetically tuned to be a superengaging motor under hindering loads. *Proc Natl Acad Sci U S A*, *120*(2), e2216903120. https://doi.org/10.1073/pnas.2216903120

Pyrpassopoulos, S., Shuman, H., & Ostap, E. M. (2020). Modulation of Kinesin's Load-Bearing Capacity by Force Geometry and the Microtubule Track. *Biophys J*, *118*(1), 243-253. https://doi.org/10.1016/j.bpj.2019.10.045

Rai, A., Pathak, D., Thakur, S., Singh, S., Dubey, A. K., & Mallik, R. (2016). Dynein Clusters into Lipid Microdomains on Phagosomes to Drive Rapid Transport toward Lysosomes. *Cell*, *164*(4), 722-734. https://doi.org/10.1016/j.cell.2015.12.054

Rai, A. K., Rai, A., Ramaiya, A. J., Jha, R., & Mallik, R. (2013). Molecular adaptations allow dynein to generate large collective forces inside cells. *Cell*, *152*(1-2), 172-182. https://doi.org/10.1016/j.cell.2012.11.044

Rao, L., & Gennerich, A. (2022). Single-Molecule Studies on the Motion and Force Generation of the Kinesin-3 Motor KIF1A. *Methods Mol Biol*, *2478*, 585-608. https://doi.org/10.1007/978-1-0716-2229-2_21

Reid, E., Kloos, M., Ashley-Koch, A., Hughes, L., Bevan, S., Svenson, I. K., Graham, F. L., Gaskell, P. C., Dearlove, A., Pericak-Vance, M. A., Rubinsztein, D. C., & Marchuk, D. A. (2002). A kinesin heavy chain (KIF5A) mutation in hereditary spastic paraplegia (SPG10). *Am J Hum Genet*, *71*(5), 1189-1194. https://doi.org/10.1086/344210

Ruhnow, F., Zwicker, D., & Diez, S. (2011). Tracking single particles and elongated filaments with nanometer precision. *Biophys J*, *100*(11), 2820-2828. https://doi.org/10.1016/j.bpj.2011.04.023

Sanghavi, P., Kumar, P., Roy, A., Madhusudhan, M. S., & Mallik, R. (2021). On and off controls within dynein-dynactin on native cargoes. *Proc Natl Acad Sci U S A*, *118*(23). https://doi.org/10.1073/pnas.2103383118

Schnitzer, M. J., Visscher, K., & Block, S. M. (2000). Force production by single kinesin motors. *Nat Cell Biol*, *2*(10), 718-723. https://doi.org/10.1038/35036345

Schroeder, H. W., 3rd, Hendricks, A. G., Ikeda, K., Shuman, H., Rodionov, V., Ikebe, M., Goldman, Y. E., & Holzbaur, E. L. (2012). Force-dependent detachment of kinesin-2 biases track switching at cytoskeletal filament intersections. *Biophys J*, *103*(1), 48-58. https://doi.org/10.1016/j.bpj.2012.05.037

Siddiqui, N., Roth, D., Toleikis, A., Zwetsloot, A. J., Cross, R. A., & Straube, A. (2022). Force generation of KIF1C is impaired by pathogenic mutations. *Curr Biol*, *32*(17), 3862-3870 e3866. https://doi.org/10.1016/j.cub.2022.07.029

Soppina, P., Patel, N., Shewale, D. J., Rai, A., Sivaramakrishnan, S., Naik, P. K., & Soppina, V. (2022). Kinesin-3 motors are fine-tuned at the molecular level to endow distinct mechanical outputs. *BMC Biol*, *20*(1), 177. https://doi.org/10.1186/s12915-022-01370-8

Soppina, V., Norris, S. R., Dizaji, A. S., Kortus, M., Veatch, S., Peckham, M., & Verhey, K. J. (2014). Dimerization of mammalian kinesin-3 motors results in

superprocessive motion. *Proc Natl Acad Sci U S A*, *111*(15), 5562-5567. https://doi.org/10.1073/pnas.1400759111

Soppina, V., Rai, A. K., Ramaiya, A. J., Barak, P., & Mallik, R. (2009). Tug-of-war between dissimilar teams of microtubule motors regulates transport and fission of endosomes. *Proc Natl Acad Sci U S A*, *106*(46), 19381-19386. https://doi.org/10.1073/pnas.0906524106

Soppina, V., & Verhey, K. J. (2014). The family-specific K-loop influences the microtubule on-rate but not the superprocessivity of kinesin-3 motors. *Mol Biol Cell*, *25*(14), 2161-2170. https://doi.org/10.1091/mbc.E14-01-0696

Sudhakar, S., Abdosamadi, M. K., Jachowski, T. J., Bugiel, M., Jannasch, A., & Schaffer, E. (2021). Germanium nanospheres for ultraresolution picotensiometry of kinesin motors. *Science*, *371*(6530). https://doi.org/10.1126/science.abd9944

Svoboda, K., & Block, S. M. (1994). Force and velocity measured for single kinesin molecules. *Cell*, *77*(5), 773-784. https://doi.org/10.1016/0092-8674(94)90060-4

Thomas, W. E., Trintchina, E., Forero, M., Vogel, V., & Sokurenko, E. V. (2002). Bacterial adhesion to target cells enhanced by shear force. *Cell*, *109*(7), 913-923. https://doi.org/10.1016/s0092-8674(02)00796-1

Thomas, W. E., Vogel, V., & Sokurenko, E. (2008). Biophysics of catch bonds. *Annu Rev Biophys*, *37*, 399-416. https://doi.org/10.1146/annurev.biophys.37.032807.125804

Toleikis, A., Carter, N. J., & Cross, R. A. (2020). Backstepping Mechanism of Kinesin-1. *Biophys J*, *119*(10), 1984-1994. https://doi.org/10.1016/j.bpj.2020.09.034

Tomishige, M., Klopfenstein, D. R., & Vale, R. D. (2002). Conversion of Unc104/KIF1A kinesin into a processive motor after dimerization. *Science*, *297*(5590), 2263-2267. https://doi.org/10.1126/science.1073386

Uemura, S., Kawaguchi, K., Yajima, J., Edamatsu, M., Toyoshima, Y. Y., & Ishiwata, S. (2002). Kinesin-microtubule binding depends on both nucleotide state and loading direction. *Proc Natl Acad Sci U S A*, *99*(9), 5977-5981. https://doi.org/10.1073/pnas.092546199

Valentine, M. T., & Block, S. M. (2009). Force and premature binding of ADP can regulate the processivity of individual Eg5 dimers. *Biophys J*, *97*(6), 1671-1677. https://doi.org/10.1016/j.bpj.2009.07.013

Visscher, K., Schnitzer, M. J., & Block, S. M. (1999). Single kinesin molecules studied with a molecular force clamp. *Nature*, *400*(6740), 184-189. https://doi.org/10.1038/22146

Welte, M. A. (2004). Bidirectional transport along microtubules. *Curr Biol*, *14*(13), R525-537. https://doi.org/10.1016/j.cub.2004.06.045

Woody, M. S., Lewis, J. H., Greenberg, M. J., Goldman, Y. E., & Ostap, E. M. (2016). MEMLET: An Easy-to-Use Tool for Data Fitting and Model Comparison Using Maximum-Likelihood Estimation. *Biophys J*, *111*(2), 273-282. https://doi.org/10.1016/j.bpj.2016.06.019

Yildiz, A., Tomishige, M., Gennerich, A., & Vale, R. D. (2008). Intramolecular strain coordinates kinesin stepping behavior along microtubules. *Cell*, *134*(6), 1030-1041. https://doi.org/10.1016/j.cell.2008.07.018

Zaniewski, T. M., Gicking, A. M., Fricks, J., & Hancock, W. O. (2020). A kinetic dissection of the fast and superprocessive kinesin-3 KIF1A reveals a predominant one-

head-bound state during its chemomechanical cycle. *J Biol Chem*, *295*(52), 17889-17903. https://doi.org/10.1074/jbc.RA120.014961

Zaniewski, T. M., & Hancock, W. O. (2023). Positive charge in the K-loop of the kinesin-3 motor KIF1A regulates superprocessivity by enhancing microtubule affinity in the one-head-bound state. *J Biol Chem*, *299*(2), 102818. https://doi.org/10.1016/j.jbc.2022.102818

Zhou, Y., Xu, M. F., Chen, J., Zhang, J. L., Wang, X. Y., Huang, M. H., Wei, Y. L., & She, Z. Y. (2024). Loss-of-function of kinesin-5 KIF11 causes microcephaly, chorioretinopathy, and developmental disorders through chromosome instability and cell cycle arrest. *Exp Cell Res*, *436*(1), 113975. https://doi.org/10.1016/j.yexcr.2024.113975

Supporting Information for

DNA tensiometer reveals catch-bond detachment kinetics of kinesin-1, -2 and -3

Crystal R. Noell[1], Tzu-Chen Ma[1], Rui Jiang[1], Scott Mckinley[2], William O. Hancock*[1,3]

* Corresponding author.
Email: woh1@psu.edu

Supplementary Methods

Biotinylated MT

Tubulin was purified from bovine brain as previously described (Cleary et al., 2022; Uppalapati M, 2009), with the following modifications. After the 45 minute growth phase a 12-fold excess of EZ-link NHS-biotin (Thermo Fisher 20217) was added and incubation at 37℃ continued for another 30 minutes. Microtubules were then depolymerized, polymerized, and pelleted twice to obtain pure biotinylated tubulin. Tubulin concentration was measured by absorbance, and the fraction biotinylated measured using the Biocytin Kit (Thermo Fisher 28022).

Motor Expression, Purification and Oligo Conjugation

Drosophila melanogaster Kinesin-1-EGFP-SNAP-His_6 (aa 1-406) was expressed in Tuner (DE3) E.coli (Addgene #129764). Cells were grown in Terrific Broth (Sigma Aldrich) at 37℃ with shaking at 180 rpm for 4-6 hours until an OD of greater than 1 was reached, then induced with 120 mg IPTG and shaken overnight at 21℃. Cells were harvested the next day, pelleted, resuspended with 1x PBS, frozen, and stored at -80℃. *Rattus norvegicus* Kif1A (aa 1-351)-Kif1A neck linker (NL) (17aa)-Kinesin1 coiled-coil (aa 345-406)-EGFP-SNAP was expressed in Tuner (DE3) E.coli similarly to kinesin-1 (Addgene #229851). *Mus musculus* Kif3A (aa 1-342)-Kif3A NL (17aa)-Kinesin1 coiled-coil (aa 345-406)-EGFP-SNAP was expressed in BL21(DE3) E.coli (Addgene # 229852). Kif1A and Kif3A constructs were synthesized into the kinesin-1 construct backbone by GenScript. His_6 tagged GBP-SNAP in pet28a was also expressed and purified similarly (Feng et al., 2020; Feng et al., 2018; Gicking et al., 2022; Kubala et al., 2010).

Bacterial cell pellets (from 800 mL culture) were thawed and motors were purified via Ni affinity chromatography as described previously (Gicking et al., 2022; Gicking et al., 2019; Zaniewski et al., 2020). Motor proteins were eluted in a buffer containing 20 mM phosphate buffer, 500 mM sodium chloride, 500 mM imidazole, 10 μM ATP and 5 mM DTT. The concentration of pre-labeled motors was then measured by absorbance at 488 nm (using the EGFP extinction coefficient 55,900 $M^{-1}cm^{-1}$), and proteins were visualized with SDS PAGE.

Amine-terminated oligonucleotides (IDT) were resuspended and desalted into 200 mM sodium borate buffer, and the concentration measured by absorbance. The desalted oligo was then mixed with 20-fold excess of BG-GLA-NHS (NEB S9151S, dissolved in DMSO) in 100 mM sodium borate and 50% DMSO and incubated at RT for 30 min. The mixture was then desalted into 1x PBS buffer (containing 1 mM DTT and 1 mM $MgCl_2$). The elution profile was measured by absorbance and the fractions of BG-oligo were pooled. The pre- and post- labeled oligos were visualized on a 10% TBE-Urea gel and stained with SYBR green I. Excess BG-oligo was stored at -20℃.

Immediately following Ni column purification of motors, BG-oligo was mixed with the eluted motor at a 5:1 ratio and incubated on ice for 1 hr. The mixture was then diluted with 1x PBS + 1 mM $MgCl_2$ sufficient to reduce the imidazole concentration to below 80 mM, and a second Ni-affinity purification was carried out to remove the excess BG-oligo. The protein was eluted in the same elution buffer and flash frozen in liquid N_2 in the presence of 10 μM MgATP, 1 mM DTT and 10% sucrose. Final protein

concentration was measured by EGFP absorbance. SDS-PAGE and native PAGE were used to estimate the percentage of motors that have an oligo conjugated to them, typically ~50% were labeled. Oligo-labeled motors were kept at -80℃ for up to a year.

QDot Labeling

For labelling GFP motors, Qdots were functionalized with GFP-binding protein (GBP) as follows. QDot® ITKTM Amino (PEG) quantum dots (Thermo Fisher Q21541MP) were buffer exchanged by transferring 250uL into a 100K ultrafiltration unit and adding 1x PBS pH 7.4 to make up the filter volume of 4 mL. The sample was centrifuged to the original volume of 250 μL before more buffer was added and the process was repeated 3x. The Qdots were then transferred to a glass vial, BG-GLA-NHS was added in 50-fold excess in a 100 mM sodium borate buffer containing 50% DMSO (v/v), and the reaction incubated for 1 hr at room temperature on a rotator. Excess BG-GLA-NHS was removed by carrying out 5 complete buffer exchanges with a 100K centrifugal concentrating filter. The concentration of BG-Qdots was determined on a plate reader based on a calibration curve from the initial Qdot stock. BG-Qdots were then mixed with GBP-SNAP at a 1:50 ratio and incubated on ice for 1 hour. Qdot-GBP was stored at 4℃ for up to 6 months. On the day of an experiment, Qdot-GBP was mixed with GFP labeled motors at a 10:1 ratio to prevent multi-motor Qdots and incubated on ice for at least 15 minutes before visualization by TIRF.

Fitting Equations

Data in Figures 2, S5 and S6 were fit using MEMLET (Woody et al., 2016) to the following single exponential function:

$$\boldsymbol{y(t) = \frac{k e^{-kt}}{e^{-k t_{min}}}}$$

where *k* is the rate constant (inverse of the time constant) and t_{min} is the minimum cutoff of the distribution.

Data in Figure S4 were fit using MEMLET to the following bi-exponential function:

$$\boldsymbol{y(t) = \frac{\left(A k_1 e^{-k_1 t} + (1-A) k_2 e^{-k_2 t}\right)}{\left(A e^{-k_1 t_{min}}\right) + \left((1-A) e^{-k_2 t_{min}}\right)}}$$

Here A is the amplitude of the first phase, k_1 and k_2 are the rate constants (inverse time constants) of the two phases, and t_{min} is the minimum cutoff of the distribution. This approach corrects the amplitudes for missed events, which can differ for the two phases Cumulative distribution data in Figure 4 were fit by least squares in Matlab to the bi-exponential function:

$$\boldsymbol{y(t) = A_1\left(1 - e^{-\frac{(x-t_0)}{\tau_1}}\right) + (1-A_1)\left(1 - e^{-\frac{(x-t_0)}{\tau_2}}\right)}$$

Here $\boldsymbol{\tau_1}$ and $\boldsymbol{\tau_2}$ are time constants (inverse rate constants) of the two phases, A_1 is the amplitude of the first phase, and t_0 is the minimum cutoff time of the distribution. Amplitudes are normalized to account for missed short events as follows:

$$\boldsymbol{A_{1_{corrected}} = A_1 e^{\frac{t_0}{\tau_1}}}$$

$$\boldsymbol{A_{2_{corrected}} = (1 - A_1) e^{\frac{t_0}{\tau_2}}}$$

$$\boldsymbol{A_{1_{corrected_{relative}}} = \frac{A_{1_{corrected}}}{A_{1_{corrected}} + A_{2_{corrected}}}}$$

$$\boldsymbol{A_{2_{corrected_{relative}}} = \frac{A_{2_{corrected}}}{A_{1_{corrected}} + A_{2_{corrected}}}}$$

Inference strategy for the ramp duration parameter

The primary challenge in assessing ramp runs is that these segments can end for one of two reasons: either (1) the motor detaches, or (2) the motor reaches a distance sufficiently far from the anchor to enter a stalled state. By contrast, unloaded runs and stall segments all end in detachments from microtubules. So, while taking a simple average of segment durations will result in an "average time until detachment" for unloaded and stalled segments, this is not the case for ramps. Moreover, ambiguity as to when a ramp run begins further confirms that a simply average of ramp segment durations will lead to errors. This issue is similar to the one raised in Rayens et al. (Rayens et al., 2022) in which the authors sought to estimate the average stationary segment length for motor-lysosome complexes in vivo, even though the length of some stationary segments exceeded the length of the observation window.

One way to address the problem of truncated durations is to assume that state-switching satisfies the Markov property, which is to say that whether an agent switches states in a given time step is independent of states and switches that occurred during previous time steps. for continuous time Markov chains, models are expressed in terms of rates, and so the natural quantity of interest here is the detachment rate, which might commonly be denoted k_{off}. Within the text, we wish to compare ramp state properties to unloaded and stall states which are quantified in terms of their average duration. In this note we therefore write the detachment rate in terms of a duration parameter $\tau = 1/k_{\text{off}}$. Generically, the probability that a continuous-time Markov chain does not change state in a segment of time $[a, b]$ is given by the formula:

$$P(\text{No change during [a, b]}) = e^{-\int_a^b \kappa(t)dt},$$

where $\kappa(t)$ the (possibly evolving) rate at which changes occur. If we assume that the detachment rate $1/\tau$ is constant, then in any segment of length Δ, the probability that a motor does not detach is

$$P(\text{No change during [a, b]}) = e^{-\frac{\Delta}{\tau}},$$

Suppose that $(t_0, t_1, \ldots, t_n)$ are observation times of a tensiometer run and let T denote the time that a motor would detach were it not for transitions to stall. Then the probability that a detachment occurs in the interval $[t_k, t_{k+1})$ is product of the probabilities it does not detach in all preceding segments multiplied by the probability it does detach in the final one. This idea is shown in the diagram below. The initial green segments are ramps which may result in a detachment (yellow star), or

result in conversion to a stall state (red line) which always ends in a detachment. In describing our approach to inference, we denote the ramp durations $\{T_i\}_{i=1}^{N+M}$ and the stall durations are $\{S_i\}_{i=1}^{M}$. This notation scheme implies that there were *N* detachment events during ramp segments.

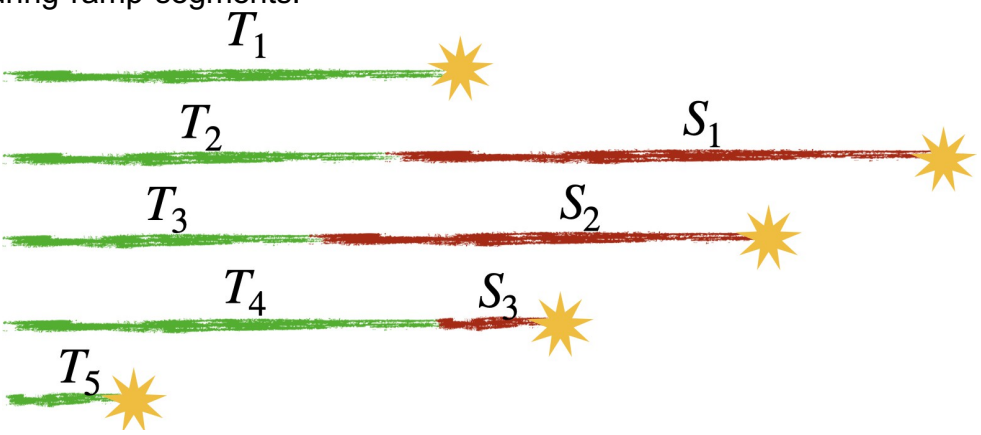

Mathematically, we write

$$P\big(T \in [t_k, t_{k+1})\big) = \Big(\prod_{i=1}^{k} e^{\frac{-(t_i - t_{i-1})}{\tau}}\Big)\left(1 - e^{\frac{-(t_{k+1} - t_k)}{\tau}}\right)$$
$$= e^{-\frac{-(t_k - t_0)}{\tau}}\left(1 - e^{\frac{-(t_{k+1} - t_k)}{\tau}}\right)$$

Assuming that time increments are evenly spaced and of size Δ, and also assuming that Δ is small compared to the duration parameter τ, we can take the first term of the Taylor expansion of the $(t_{k+1} - t_k)$ term and simplify:

Ramp with detachment: $P\big(T \in [t_k, t_{k+1})\big) \approx e^{\frac{-(t_k - t_0)}{\tau}}\frac{\Delta}{\tau}$

On the other hand, suppose that the motor switches to a stalled state after time t_k. Then the initial product of non-detaching segments remains the same, and final term is removed:

Ramp without detachment: $P\big(T \in [t_k, t_{k+1})\big) \approx e^{\frac{-(t_k - t_0)}{\tau}}$

To unify the notation, let 1_i^{det} denote the event that the *i* ramp run detached before reaching stall phase. We have

$$P\big(T \in [t_k, t_{k+1})\big) \approx \left(\frac{\Delta}{\tau}\right)^{1_i^{det}} e^{\frac{-(t_k - t_0)}{\tau}}$$

To perform inference on multiple runs, we assume they are independent and so, again, we can take a simple product. As described in the caption of Figure 1, let $\{T_i\}_{i=1}^{N+M}$ be an enumeration of ramp durations, where *N* is the number of ramps that detached and *M* is the number of ramps that reached a stall state. It follows that the likelihood of observing a set of trajectories *X* given a duration parameter τ can be written

$$P(X;\tau) = \prod_{i=1}^{N+M}\left(\frac{\Delta}{\tau}\right)^{1_i^{det}} e^{\frac{-T_i}{\tau}}$$
$$= \left(\frac{\Delta}{\tau}\right)^{N} e^{\frac{-\sum T_i}{\tau}}$$

From a Bayesian perspective, we can use this likelihood function to create a posterior distribution for the duration parameter τ. In this work we have used a scale-free uninformative prior (Robert, 1994) of the form $\pi(r) = r^{-1}$. Together with the likelihood, we have that the posterior distribution has the form

$$\pi(\tau|X) \overset{c}{=} P(X;\tau)\pi(\tau)$$
$$= \Delta^N \tau^{-(N+1)} e^{\frac{-\sum T_i}{\tau}}$$

where $\overset{c}{=}$ means "equals up to a constant depending only on X". Looking at the factors that depend only on τ this is an Inverse Gamma distribution.
In this way, we reach the conclusion that if T is the total time spent in the ramp states and if N is the number of detachments while in the ramp state, the posterior distribution for the duration parameter is

$$\pi(\tau|T,N) \sim \text{InvGamma}(N, T).$$

This means that it has pdf

$$f(t;N,T) = \frac{T^N}{\Gamma(N)} \frac{1}{t^{\alpha+1}} e^{\frac{-T}{\tau}}$$

and, most importantly for the purpose of estimation, the mean of the posterior distribution is simply T/N. In other words, the simple Bayes estimator for a collection of ramp segments is:

$$\hat{\tau} = \frac{T}{N} = \frac{\text{Total time in ramp phase}}{\text{Number of detachments in ramp phase}}$$

To set our $100(1-\alpha)$ %-credible regions, we used the middle-α probability range from the posterior distribution. This means that the 95% credible region is defined as the interval between the 0.025-quantile and 0.975-quantile of the posterior distribution. These regions are indicated as solid lines segments beneath the posterior distributions depicted in Figure 3 in the main text.

Compensating for difficulty in observing short runs

For unloaded and ramp runs there is a significant risk that short runs will be unobserved. For ramp runs, short ramp phases might be masked by the fluctuations that occur when the motor is detached. Meanwhile, short, unloaded runs might not be recognized among many motors in a wide field of view. Among kinesin-1 runs, for example, the shortest recorded unloaded run was 0.48s, despite the frame rate being significantly smaller. The minimum recorded times, t_{min} (seconds), for each category of run observations is as follows:

	Stall	Ramp	Unloaded
Kinesin-1	0.1	0.14	0.48
Kinesin-2	0.22	0.17	0.348
Kinesin-3	0.03	0.03	0.641

The likelihood function therefore needs to be adjusted to be conditioned on being greater than the minimum observation time for that cohort. Continuing with the notation from above (for convenience taking $t_0 = 0$, let T_i denote the ith run duration. Then the joint likelihood function is therefore

$$P(T \in [t_k, t_{k+1}) | T_i > t_{\min}) = \frac{P(T \in [t_k, t_{k+1}), T_i > t_{\min})}{P(T_i > t_{\min})}$$

$$\approx \frac{1_{t_k > t_{\min}} e^{\frac{-t_k}{\tau}} \Delta}{e^{\frac{-t_{\min}}{\tau}}}$$

$$= 1_{t_k > t_{\min}} e^{\frac{-(t_k - t_{\min})}{\tau}} \frac{\Delta}{\tau}$$

For a collection of paths χ, the likelihood function becomes

$$P(X | \tau, t_{\min}) = \prod_{i=1}^{N+M} 1_{T_i > t_{\min}} \left(\frac{\Delta}{\tau}\right)^{1_i^{det}} e^{\frac{-(T_i - t\_\min)}{\tau}}$$

$$= 1_{\min_i T_i > t_{\min}} \left(\frac{\Delta}{\tau}\right)^{N} e^{\frac{-(T_i - t\_\min)}{\tau}}$$

Note that for any fixed value τ, the maximum of the likelihood function over all $t_{\min}$ values is $t_{\min} = \min_i T_i$. Rather than constructing a joint Bayesian posterior for the pair (τ, $t_{\min}$), we simply adopted the maximum likelihood value for $t_{\min}$ within each cohort and proceeded as described above with the likelihood function

$$P(X; \tau) \left(\frac{\Delta}{\tau}\right)^{N} e^{\frac{-\sum_i (T_i - \min_j T_j)}{\tau}}$$

1

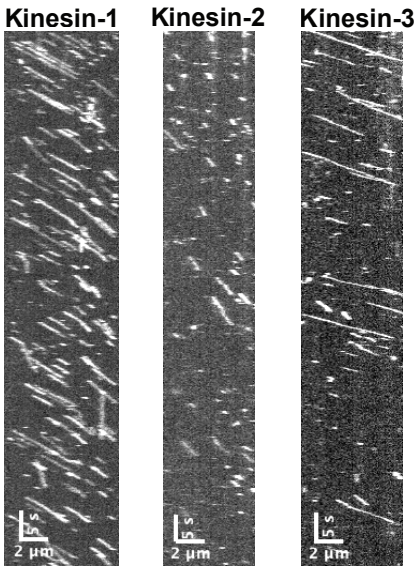

Figure. S1. Kymographs of unloaded GFP-labeled kinesins. GPF-labeled motors conjugated to their complimentary oligo were visualized via TIRF at a concentration of 1 nM at 5 fps. No neutravidin, Qdot or DNA are present in these unloaded controls. Of note, a portion of kinesin-3 unloaded run durations were limited by the length of the microtubules, meaning the unloaded duration is a lower limit.

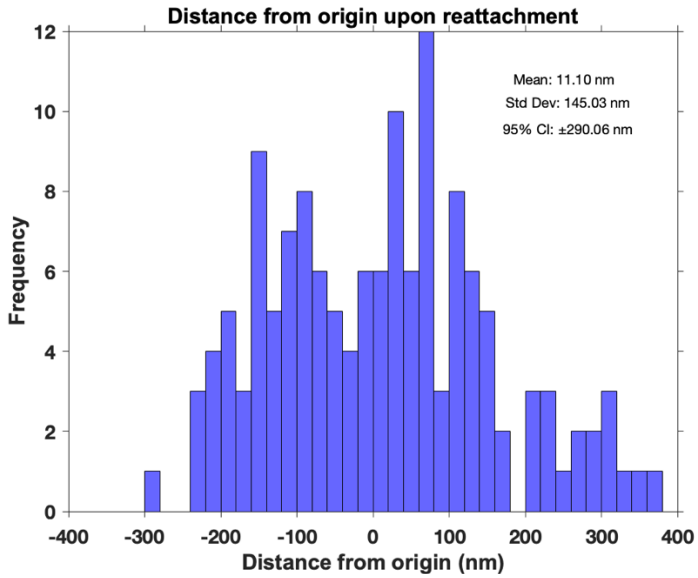

Figure. S2. Distribution of initial motor binding positions. The initial positions were measured for events where the motor was clearly dissociated from the microtubule and fluctuated around origin on its DNA tether (N=141). The zero position was determined as the center point around which the detached motor fluctuated. The initial motor binding position was determined by the first start point of a ramp. The width of the gaussian distribution, quantified by the SD, demonstrates the large search space of the motor attached to the flexible ~1-micron dsDNA tether. The mean of +11 nm likely results from some of the motors moving before the first frame acquisition, giving a small positive bias. The larger population seen at >+200 nm relative to <-200 nm may result from dissociation of motors that bind under assisting loads (negative displacements) and strengthening of motors that bind under hindering loads (positive displacements). Data are from kinesin-1 and kinesin-3 tensiometers.

Table S1. Fit results for unloaded, ramp, and stall durations

		Results from a Maximum Likelihood Estimator (MEMLET) (Fig. 2)		Results from Markov model coupled with Bayesian inference (Fig. 3)	
Motor	**State**	**τ (s)**	**95% CI (s)**	**τ (s)**	**95% CI (s)**
Kinesin-1	Unloaded	1.04	0.79 – 1.30	1.05	0.81 – 1.36
	Ramp			2.49	1.87 – 3.32
	Stall	3.01	2.30 – 3.79	3.05	2.43 – 3.83
Kinesin-2	Unloaded	1.07	0.85 – 1.35	1.09	0.88 – 1.34
	Ramp			0.97	0.87 – 1.08
	Stall	2.83	2.03 – 3.79	2.90	2.17 – 3.86
Kinesin-3	Unloaded	2.74	2.33 – 3.17	2.76	2.28 – 3.34
	Ramp			0.75	0.64 – 0.87
	Stall	1.89	1.53 – 2.31	1.90	1.60 – 2.25

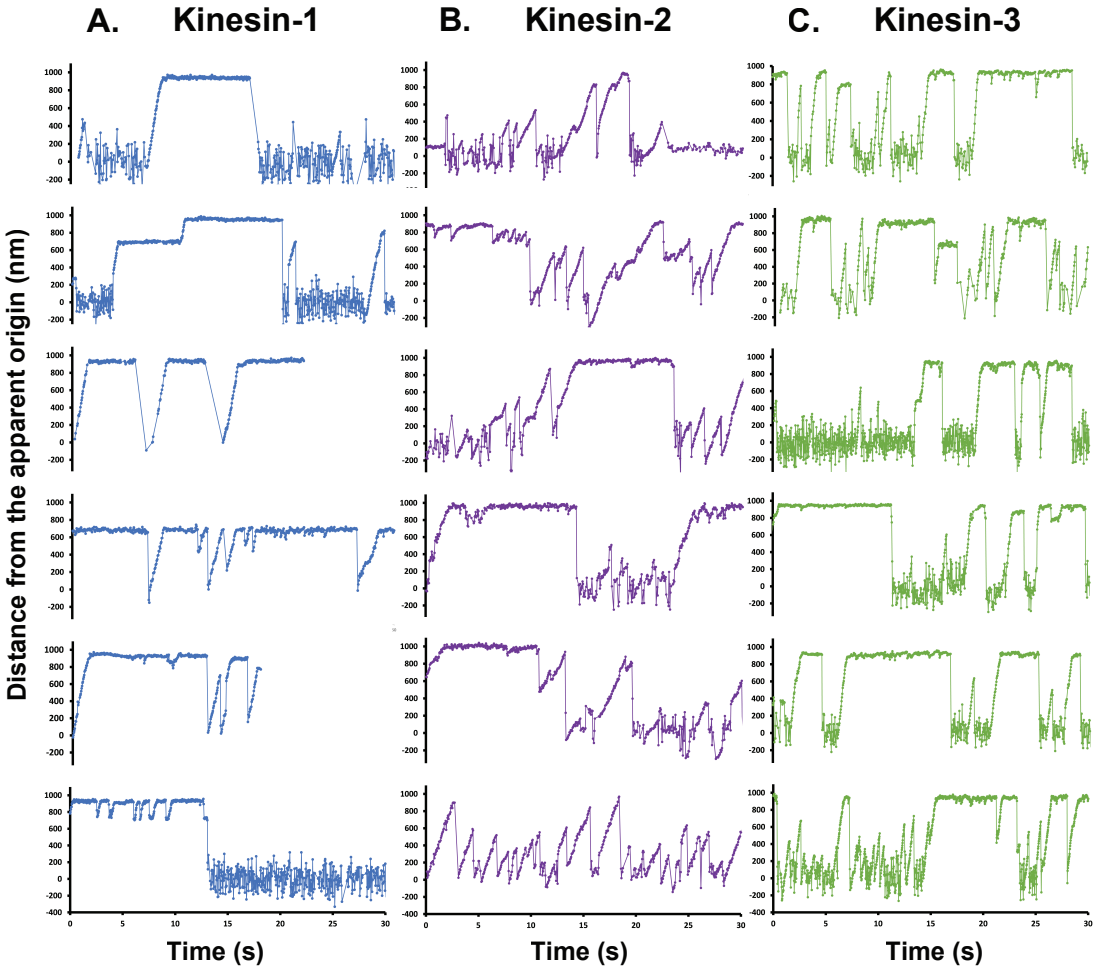

Figure. S3. Further kinesin tensiometer examples. Distance versus time plots of (A) kinesin-1, (B) kinesin-2 and (C) kinesin-3 traces. Notably, some stalls are very stable, whereas other (particularly for kinesin-2 and kinesin-3) show fluctuations, presumably due to small slips and backstepping at stall. Other features to note include pauses in the motile segments, small changes in velocity, and repeated ramps for kinesin-2. Roughly 20% of our tensiometers extended less than the expected 1 μm distance, stalling repeatedly at 500 nm or 800 nm. These apparently shorter DNA strands may result from DNA secondary structures or from primer binding at a secondary sequence. After in-depth comparison of the data we found that the stall durations, reattachment rates, and starting positions were unaffected by the shorter DNA length and thus included the shorter tensiometers in our data set.

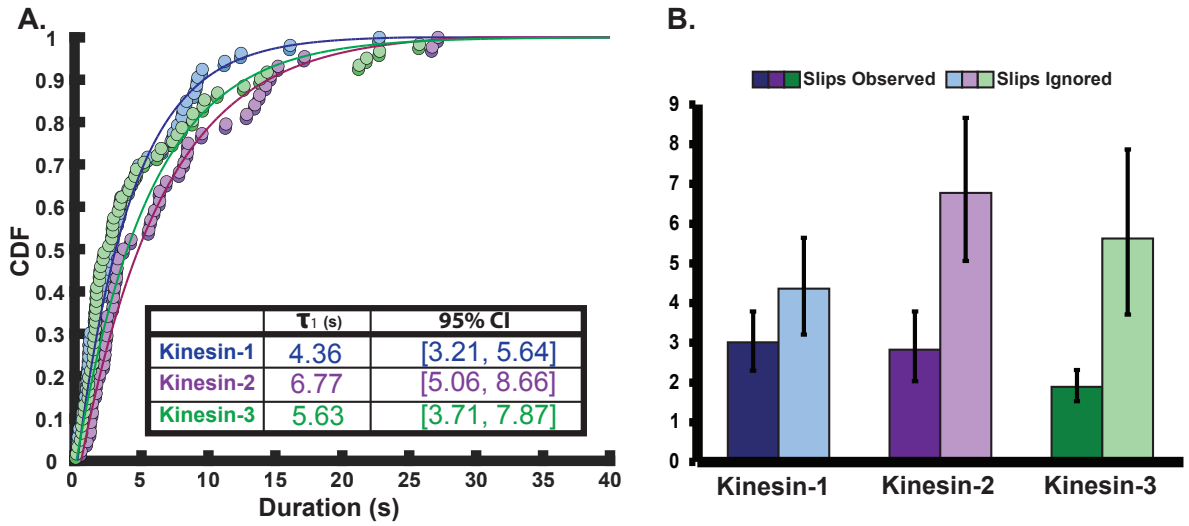

Figure. S4. Stall durations ignoring transient slip events at stall. In our stall duration analysis in Figure 2, we defined transient slip events, when the motor slips backward but not all the way to the origin, as terminating a stall plateau. However, functionally, such as in a tug-of-war with dynein, these slip events will only cause a transient displacement, and the motor will then rapidly reestablish a stall. Thus, they can be considered simply as fluctuations with the true end of a stall being when the motor returns to the origin, denoting full motor detachment. To quantify this functional stall duration, we ignored slip events and defined the end of stalls as the motor returning to the origin. (A) The CDF of these 'functional stall' durations was fit with a single exponential function using a maximum likelihood estimator (MEMLET). The resulting time constants are shown in the inset table. (B) A bar plot comparing time constants, where stalls are not ended by slips, and where they are. Time constants where stalls are not ended by slips were all longer than the values from Figure 2 (3.01 s, 2.83 s, and 1.89 s, respectively). The largest difference was seen for kinesin-2 and -3. The error bars are the 95% confidence intervals determined by MEMLET bootstrapping.

Table S2: Relative frequency of slips during stall plateaus.

	τ_{stall} no slips (s)	τ_{stall} with slips (s)	Ratio
Kinesin-1	3.01	4.36	1.5
Kinesin-2	2.83	6.77	2.4
Kinesin-3	1.89	5.63	3.0

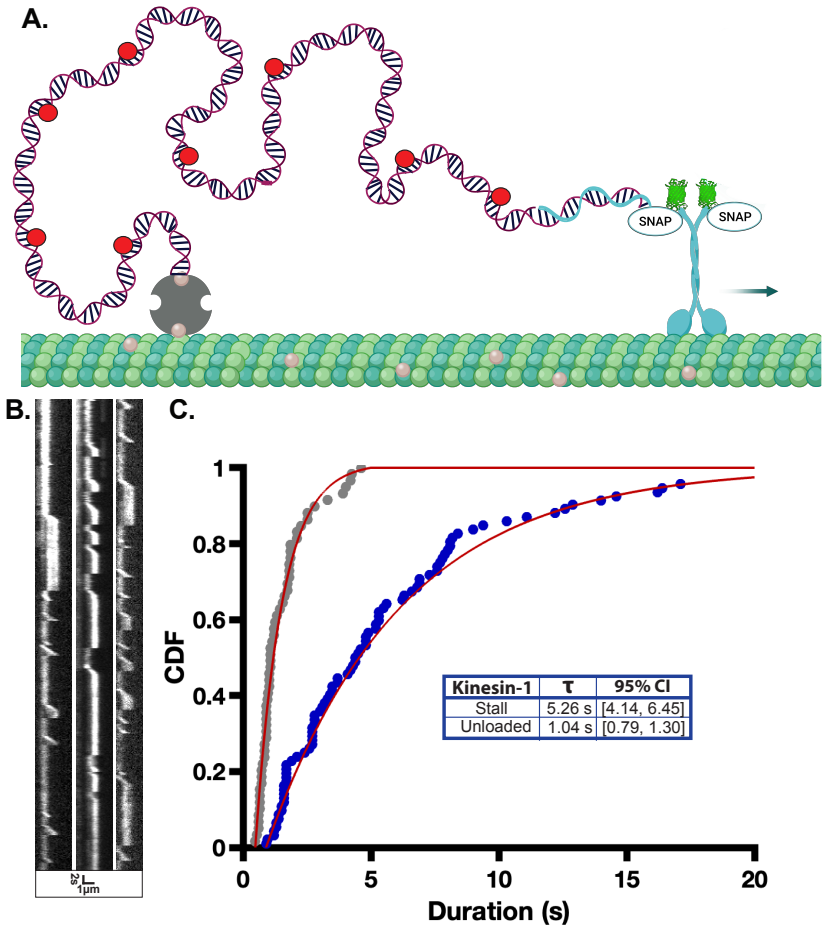

Figure. S5. Long stall durations are observed in the absence of Qdots. Because the Qdots used in our experiments are functionalized with multiple GBP nanobodies, there is the possibility that the long stall durations observed were caused by multiple motors bound to the Qdots. To test this, we ran a control experiment where, instead of labeling the motors with Qdots, we fluorescently labeled our dsDNA by incorporating 5% dCTP-Cy5 during the PCR reaction to create fluorescent dsDNA. By removing Qdots from the system, the potential for multimotor events is eliminated. (A) Diagram of control experiment. (B) TIRF kymographs of representative bright kinesin-1 DNA tensiometers collected at 5 fps, showing the typical extension and stall profiles we observed in Figure 1, with the difference that the entire dsDNA is visualized rather than the Qdot. (C) CDF plot of the fluorescent DNA tensiometer stall durations of kinesin-1, fit with a single exponential function using a maximum likelihood estimator (MEMLET). Importantly, kinesin-1 continued to have much longer stall durations than its unloaded run durations (gray points with fit; reproduced from Fig. 2A), ruling out multi-motor interactions as the cause of the long stall durations. The longer stall durations here (5.26 s) compared to the Qdot stall durations (3.01 s; Fig. 2A) is attributed to the 5 fps frame rate used in here, which makes it more difficult to detect short slip events that are observed with the 25 fps Qdot movies.

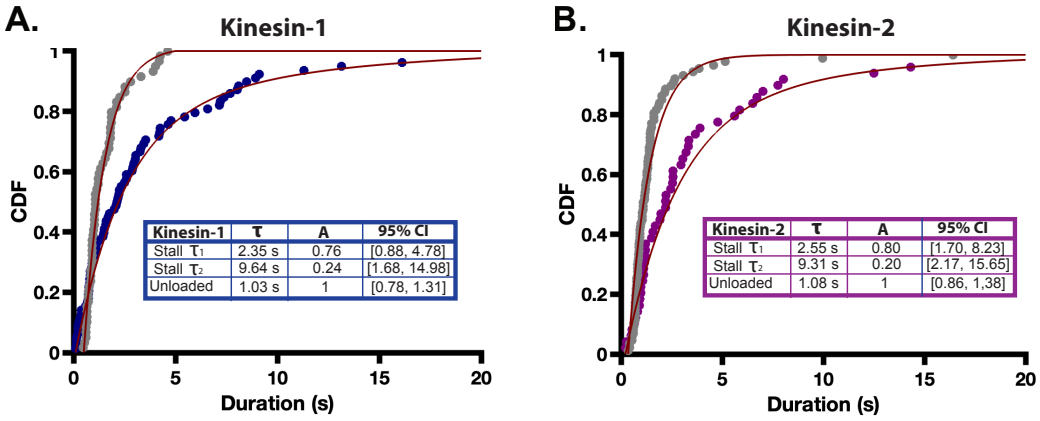

Figure. S6. Bi-exponential fits of stall durations reveal a longer duration sub-population for kinesin-1 and kinesin-2. Tensiometer stall durations of (A) kinesin-1 and (B) kinesin-2 were fit with a biexponential function using a maximum likelihood estimator, MEMLET (https://michaelswoody.github.io/MEMLET/). Unloaded run durations are shown in gray for reference. Time constants (τ), relative amplitudes (A) and 95% confidence intervals for time constants are given in the accompanying tables. The rationale for why the motors would have two time constants is not clear, but it may suggest two alternative detachment pathways. Notably, both time constants are longer than the unloaded binding duration for both motors. Kinesin-3 stall durations were well fit by a single exponential function (see Fig. 2C).

Table S3. Predicted force imposed on the motor during the ramp phase

	$v_{unloaded}$ (nm/s)	v_{ramp} (nm/s)	v_{ramp} / $v_{unloaded}$	$F_{predicted}$ (pN)*
Kinesin-1	651	572	0.88	0.72
Kinesin-2	401	324	0.81	1.14
Kinesin-3	1458	1187	0.81	1.14

*Based on linear force-velocity relationship with a 6 pN stall force

Table S4. Comparison of expected and measured fraction of ramps that reach stall.

	$\tau_{unloaded}$[a] (s)	$v_{unloaded}$[b] (nm/s)	t_{950nm}[c] (s)	Predicted stall fraction[d]	Measured stall fraction[e]	Ratio[f] (measure/predict)
Kinesin-1	1.05	651	.46	0.25	0.62	2.5
Kinesin-2	1.09	401	.37	0.11	0.14	1.3
Kinesin-3	2.76	1458	.65	0.79	0.49	0.62

[a] Unloaded run durations (Fig. 2). [b] Unloaded velocities. [c] Predicted time to reach stall (950 nm extension of dsDNA; Fig 1B) based on unloaded velocities. [d] Predicted fraction of ramps that will reach stall, calculated as: p(stall) = $e^{-\frac{t_{950nm}}{t_{unloaded}}}$. [e] Measured fraction of ramps that reach stall. [f] Ratio of expected to predicted fraction of ramps that reach stall. More kinesin-1 reach stall than predicted, suggesting off-rates during ramp are slower than unloaded. In contrast, fewer kinesin-3 ramps reach stall, suggesting that off-rates during ramp are faster than unloaded.

A.

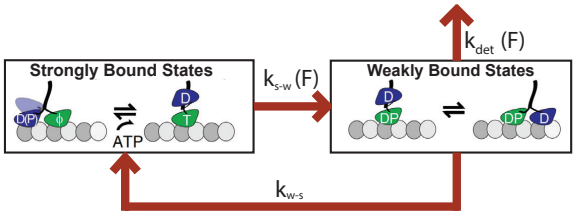

B.

Equation: $k(F) = k^0 e^{\frac{F\delta}{k_B T}}$		$k^0\ (s^{-1})$	$k_{S-W}(F)\&k_{det}(F)$ $\delta\ (nm)$
Kin1	k_{S-W}	169	-2.74
	k_{W-S}	169	-
	k_{det}	1.93	1.61
Kin2	k_{S-W}	106	-2.42
	k_{W-S}	106	-
	k_{det}	1.87	1.35
Kin3	k_{S-W}	303	-3.15
	k_{W-S}	303	-
	k_{det}	2.69	2.14

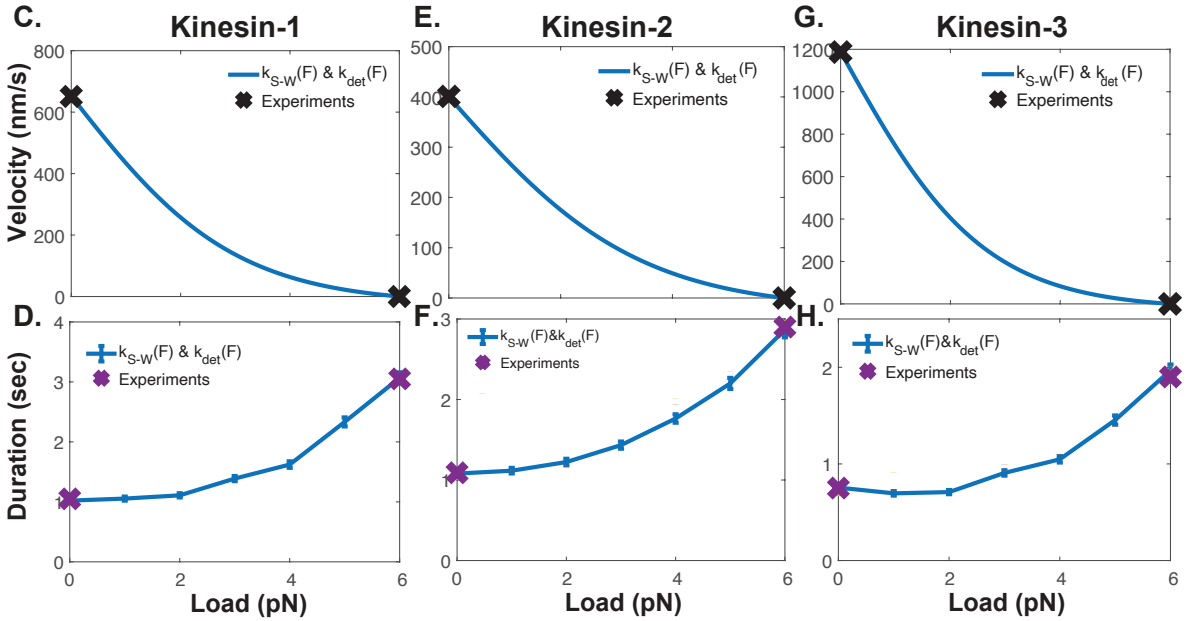

Figure. S7 Simple catch-bond model can account for all three motors. A) Diagram of $k_{S-W}(F)$ / $k_{det}(F)$ model, which is also used in Fig. 5B and C. B) Table of model parameters, where k^0 is the unloaded rate and δ is the distance parameter for each load-dependent rate constant. The two rate constants in the stepping cycle, k_{S-W} and k_{W-S} were chosen to match the unloaded velocity for each motor, and the k_{det} for each motor was chosen to match the unloaded run duration. The δ parameters for k_{S-W} were chosen such that the forward stepping rate at the 6 pN stall force was 3 s^{-1}, matching the load-independent backstepping rate. The δ parameter for k_{det} for each motor was chosen to fit the stall duration. C-H) Load dependent velocity and binding duration for kinesin-1, kinesin-2, and kinesin-3 (panel C is reproduced from Fig. 5C). Note that, based on the ramp analysis in Fig. 4 which argued that unloaded kinesin-3 runs are made up of shorter runs connected by diffusive events, we used the kinesin-3 ramp duration in panel H, rather than the unloaded run duration.

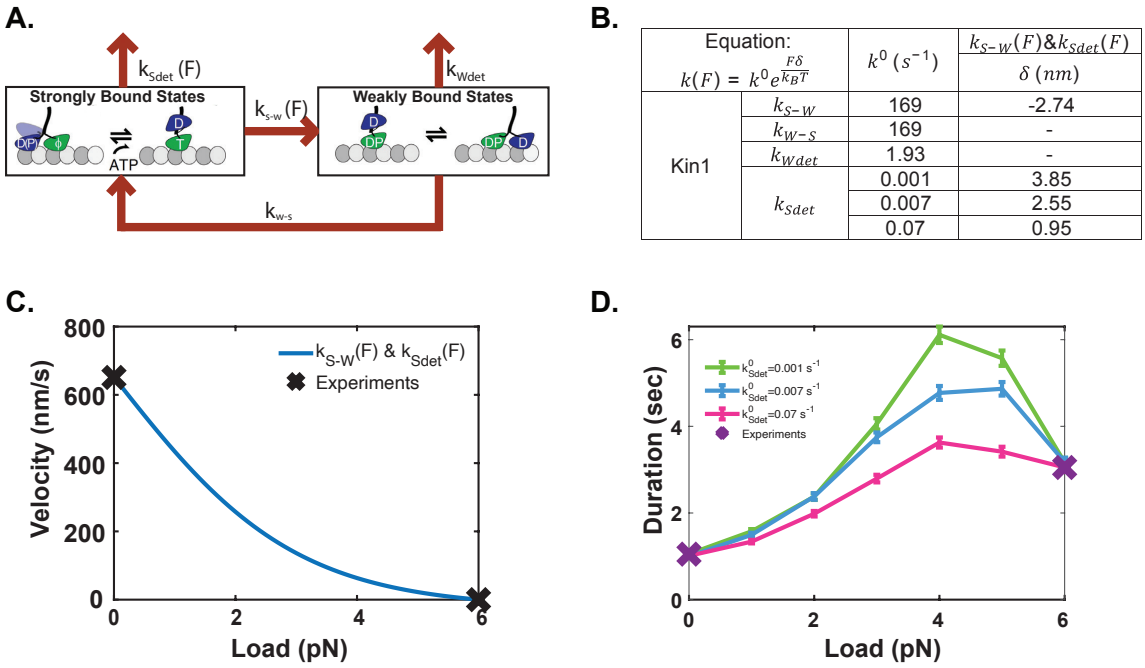

Equation: $k(F) = k^0 e^{\frac{F\delta}{k_B T}}$		$k^0\ (s^{-1})$	$k_{S-W}(F)$&$k_{Sdet}(F)$ $\delta\ (nm)$
Kin1	k_{S-W}	169	-2.74
	k_{W-S}	169	-
	k_{Wdet}	1.93	-
	k_{Sdet}	0.001	3.85
		0.007	2.55
		0.07	0.95

Figure. S8. Kinesin-1 catch-bond can also be accounted for by model incorporating load-dependent detachment from the strong-binding state. A) Diagram of $k_{S\text{-}W}$(F) / k_{Sdet}(F) model, showing the two load-dependent rate constants. B) Table of load-dependent parameters used. Unloaded k^0 for $k_{S\text{-}W}$, $k_{W\text{-}S}$, and k_{Wdet} were taken from kinesin-1 model in Fig. 5 and S7. Here, the detachment rate from the weak-binding state, k_{Wdet} (formerly called k_{det}), is load-independent, and instead k_{Sdet} is load-dependent. k_0 and δ values for k_{Sdet} were taken from estimates and measurements from Kawaguchi et al (0.001 s^{-1} and 0.007 s^{-1}) and Andreasson et al (0.07 s^{-1}) (Andreasson et al., 2015; Kawaguchi et al., 2003). In each case, the distance parameter, δ, was chosen to match the stall duration in the DNA tensiometer. As expected, slower k^0 are compensated for by larger δ. C) Force-velocity relationships are the same for all three parameter sets. D) All three models can account for the unloaded and stall durations for kinesin-1, but they each predict a different performance at intermediate loads. The reason the durations peak and fall is that at low and intermediate loads, detachment primarily occurs from the weak-binding state pathway (hence, this portion of the curve resembles the $k_{S\text{-}W}$(F) only curve in Fig. 5C), whereas at loads approaching stall, detachment occurs primarily from the strong-binding state.

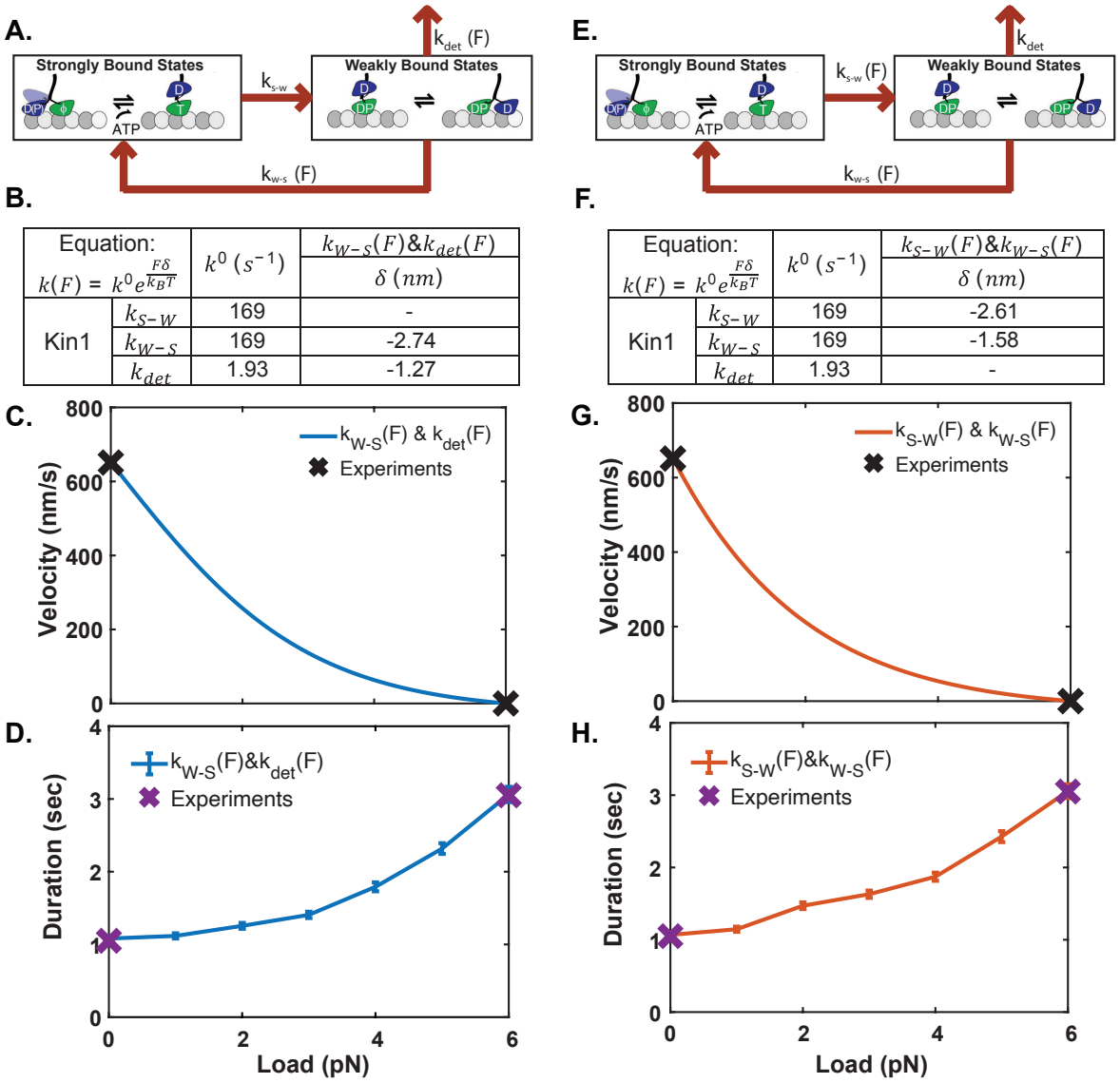

Figure. S9. Alternative models to account for catch-bond behavior. A) Diagram and B) parameters of $k_{W\text{-}S}(F)$ / $k_{det}(F)$ model. In this model, the weak-to-strong transition slows with load and the detachment rate from the weak-binding state also slows with load. In this way, detachment from the weak-binding state acts as a classic catch-bond. C and D) Load dependence of velocity and bound duration for $k_{W\text{-}S}(F)$ / $k_{det}(F)$ model. E) Diagram and F) parameters for $k_{S\text{-}W}(F)$ / $k_{W\text{-}S}(F)$ model. In this model, both transitions in the stepping cycle slow down at increasing loads, and k_{det} is load-independent. Note that $k_{S\text{-}W}$ slows with load to a greater extent than $k_{W\text{-}S}$, which results in the motor spending a greater fraction of time in the strong-binding state under load; this dynamic results in a slower motor off-rate at elevated loads. G and H) Load dependence of velocity and bound duration for $k_{S\text{-}W}(F)$ / $k_{W\text{-}S}(F)$ model.

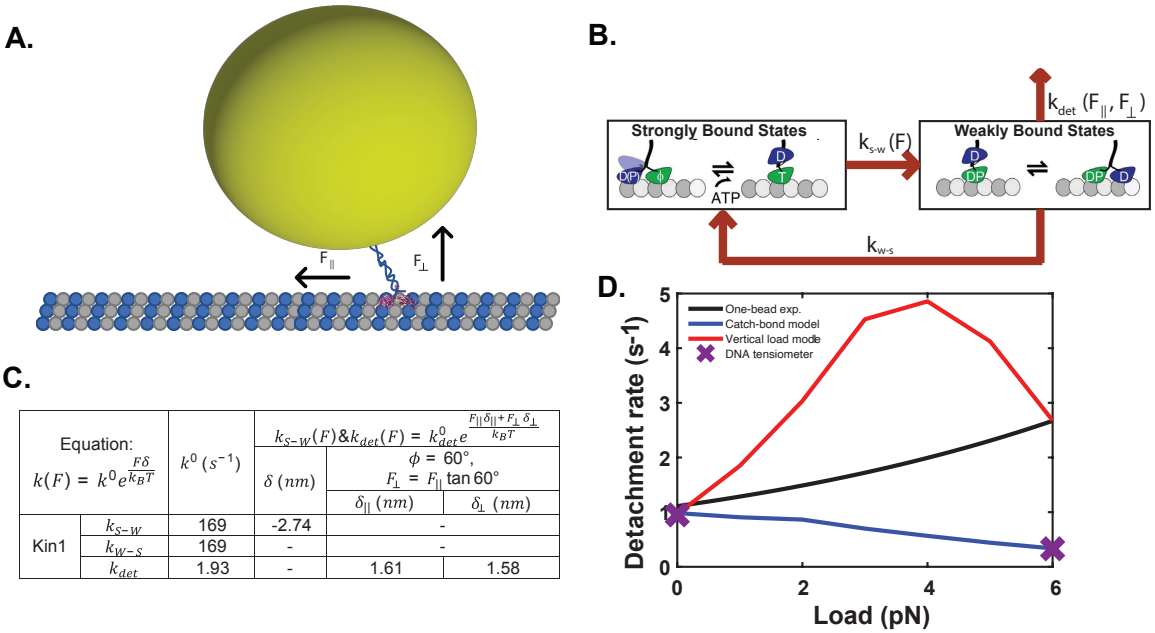

C.

Equation: $k(F) = k^0 e^{\frac{F\delta}{k_B T}}$		$k^0\ (s^{-1})$	$k_{S-W}(F)\&k_{det}(F) = k^0_{det} e^{\frac{F_\parallel \delta_\parallel + F_\perp \delta_\perp}{k_B T}}$		
			$\delta\ (nm)$	$\phi = 60°$, $F_\perp = F_\parallel \tan 60°$	
				$\delta_\parallel\ (nm)$	$\delta_\perp\ (nm)$
Kin1	k_{S-W}	169	-2.74	-	
	k_{W-S}	169	-	-	
	k_{det}	1.93	-	1.61	1.58

Figure. S10. Reconciling kinesin-1 DNA tensiometer results with published single-bead optical trapping results. A) Diagram of both perpendicular (vertical) and parallel (horizontal) forces in optical trapping studies. Note that bead (440 nm diameter) and motor (35 nm length) are not to scale. B) Diagram of model in which forces parallel to the microtubule slow $k_{S\text{-}W}$ and forces both parallel and perpendicular to the microtubule accelerate dissociation from the weak binding state, k_{det}. C) Table of parameters. Note that for k_{det}, each force component has a characteristic distance parameter, δ. These parameters have similar magnitudes, indicating that in this model, detachment has a similar sensitivity to loads oriented in the vertical versus horizontal directions. D) Comparison between simulation and experimental results for kinesin-1. Rather than duration, the detachment rate (inverse of bound duration) is plotted to enable comparison to published optical tweezer data. Purple X are DNA tensiometer results that are well fit by the model (blue line) where $F_\perp$ is zero (only forces parallel to the microtubule are involved). Note that blue detachment rate line is equivalent to bound duration from models in Fig. 5C and S7C. Black line represents experimental results from single-bead force-clamp optical tweezer results from Andreasson et al. (Andreasson et al., 2015) in which the motor angle is estimated to be 60 deg (Khataee & Howard, 2019). Equation is $k_{off}(F) = 1.11\ s^{-1} * e^{\frac{F*0.60\ nm}{4.1\ pN\ nm}}$. Red line represents model simulation results when both horizontal and vertical forces are taken into account. Note that the model captures the unloaded and stall found at the two extremities, but it overestimates the detachment rate at intermediate forces. The model dynamic that causes this overestimate is that the detachment rate rises strongly with load due to the effects of both vertical and horizontal forces, whereas the strong-to-weak transition rises more slowly with load because it is only affected by horizontal loads. Due to their exponential dependence on load, the curve peaks at intermediate loads.

SI References

Andreasson, J. O., Shastry, S., Hancock, W. O., & Block, S. M. (2015). The Mechanochemical Cycle of Mammalian Kinesin-2 KIF3A/B under Load. *Curr Biol*, *25*(9), 1166-1175. https://doi.org/10.1016/j.cub.2015.03.013

Cleary, J. M., Kim, T., Cook, A. S. I., McCormick, L. A., Hancock, W. O., & Rice, L. M. (2022). Measurements and simulations of microtubule growth imply strong longitudinal interactions and reveal a role for GDP on the elongating end. *Elife*, *11*. https://doi.org/10.7554/eLife.75931

Feng, Q., Gicking, A. M., & Hancock, W. O. (2020). Dynactin p150 promotes processive motility of DDB complexes by minimizing diffusional behavior of dynein. *Mol Biol Cell*, *31*(8), 782-792. https://doi.org/10.1091/mbc.E19-09-0495

Feng, Q., Mickolajczyk, K. J., Chen, G. Y., & Hancock, W. O. (2018). Motor Reattachment Kinetics Play a Dominant Role in Multimotor-Driven Cargo Transport. *Biophys J*, *114*(2), 400-409. https://doi.org/10.1016/j.bpj.2017.11.016

Gicking, A. M., Ma, T. C., Feng, Q., Jiang, R., Badieyan, S., Cianfrocco, M. A., & Hancock, W. O. (2022). Kinesin-1, -2, and -3 motors use family-specific mechanochemical strategies to effectively compete with dynein during bidirectional transport. *Elife*, *11*. https://doi.org/10.7554/eLife.82228

Gicking, A. M., Wang, P., Liu, C., Mickolajczyk, K. J., Guo, L., Hancock, W. O., & Qiu, W. (2019). The Orphan Kinesin PAKRP2 Achieves Processive Motility via a Noncanonical Stepping Mechanism. *Biophys J*, *116*(7), 1270-1281. https://doi.org/10.1016/j.bpj.2019.02.019

Kawaguchi, K., Uemura, S., & Ishiwata, S. (2003). Equilibrium and transition between single- and double-headed binding of kinesin as revealed by single-molecule mechanics. *Biophys J*, *84*(2 Pt 1), 1103-1113. https://doi.org/10.1016/S0006-3495(03)74926-1

Khataee, H., & Howard, J. (2019). Force Generated by Two Kinesin Motors Depends on the Load Direction and Intermolecular Coupling. *Phys Rev Lett*, *122*(18), 188101. https://doi.org/10.1103/PhysRevLett.122.188101

Kubala, M. H., Kovtun, O., Alexandrov, K., & Collins, B. M. (2010). Structural and thermodynamic analysis of the GFP:GFP-nanobody complex. *Protein Sci*, *19*(12), 2389-2401. https://doi.org/10.1002/pro.519

Rayens, N. T., Cook, K. J., McKinley, S. A., & Payne, C. K. (2022). Transport of lysosomes decreases in the perinuclear region: Insights from changepoint analysis. *Biophys J*, *121*(7), 1205-1218. https://doi.org/10.1016/j.bpj.2022.02.032

Robert, C. P. (1994). *The Bayesian Choice*. Springer.

Uppalapati M, H. Y., Shastry S, Jackson TN, Hancock WO. (2009). Methods in Bioengineering: Microfabrication and Microfluidics. In J. DZ (Ed.), (pp. 311-336).

Woody, M. S., Lewis, J. H., Greenberg, M. J., Goldman, Y. E., & Ostap, E. M. (2016). MEMLET: An Easy-to-Use Tool for Data Fitting and Model Comparison Using Maximum-Likelihood Estimation. *Biophys J*, *111*(2), 273-282. https://doi.org/10.1016/j.bpj.2016.06.019

Zaniewski, T. M., Gicking, A. M., Fricks, J., & Hancock, W. O. (2020). A kinetic dissection of the fast and superprocessive kinesin-3 KIF1A reveals a

predominant one-head-bound state during its chemomechanical cycle. *J Biol Chem*, *295*(52), 17889-17903. https://doi.org/10.1074/jbc.RA120.014961